2023

Concentration field based micropore flow rate measurements

Matia P. Edwards
Western University, medwar86@uwo.ca

Samuel F. D. J. Gómez
Western University, sgomezsu@uwo.ca

Michael S. H. Boutilier
Western University, michael.boutilier@uwo.ca

Accepted to Phys. Fluids 10.1063/5.0142808

Concentration field based micropore flow rate measurements

Matia P. Edwards,[1] Samuel F. D. J. Gómez,[2] and Michael S. H. Boutilier[3, a)]

[1)] *Graduate Research Assistant*

Mechanical and Materials Engineering

Western University

London, ON, Canada N6A 5B9

[2)] *Graduate Research Assistant*

Chemical and Biochemical Engineering

Western University

London, ON, Canada N6A 5B9

[3)] *Assistant Professor*

Chemical and Biochemical Engineering

Western University

London, ON, Canada N6A 5B9

(Dated: February 17, 2023)

Accepted to Phys. Fluids 10.1063/5.0142808

Demand is growing for a larger catalogue of experimental techniques to measure flow rates through micro/nanoscale systems for both fundamental research and device development. Flow emerging from a hole in a plane wall is a common system of interest in such work for its relevance to membrane separation. In this paper, we consider the possibility of measuring volume flow rates through small scale orifice plates from images of dye dispersions downstream. Based on approximate analytical solutions to the advection-diffusion equation, we show that, at low Reynolds numbers, the concentration in the nearly hemispherical plume that forms increases linearly with inverse distance from the pore and that the slope is proportional to volume flow rate. From micrographs of fluorescent dye plumes taken downstream of micropores of three different diameters, we demonstrate that, at Reynolds numbers below 15, the volume flow rate can be determined by extracting this slope from fluorescence intensity images. At higher Reynolds numbers, laminar jets form. In this regime, we derive an approximate similarity solution for the concentration field and show agreement of imaged dye dispersion shapes with both analytical expressions for the streamlines and isoconcentration contours at Reynolds numbers above 25. The results validate a scalable method for flow rate measurements applicable to small micropores of any geometry in plane walls and to small areas of porous materials relevant to membrane systems.

[a)]Corresponding author: michael.boutilier@uwo.ca

Accepted to Phys. Fluids 10.1063/5.0142808

I. INTRODUCTION

Nanostructured membranes have emerged as a promising class of separation technology offering enhanced permeance at comparable selectivity to conventional polymer membranes.[1–11] Membranes with nanopores defined by the inner diameter of carbon or boron nitride nanotubes,[9–18] vacancies in atomically thin graphene,[7,8,19–38] nanochannels formed between graphene oxide or other nanomaterial flakes,[5,6,39–52] or the nanoporous material structure of metal or covalent organic frameworks[53–56] have been explored for liquid and gas phase separation applications. The nanostructures in these membranes can accomplish separation through size-based sieving or through charge or chemical interactions with the pore.

Standard measurement tools for permeance and selectivity are available to characterize the performance of centimeter-scale membranes.[5–10] However, at this size, measurements are of parallel transport through trillions of pores and include flow pathways through defects present in the membrane.[57,58] For many of these types of membranes, a distribution of pore sizes will exist due to fabrication challenges, for example in producing nanotubes of the exact same diameter[59] or uniformly nucleating and growing pores in graphene.[7] This complicates optimizing or tailoring pore structures for specific applications and screening candidate membrane materials for potential performance prior to larger scale membrane development.

Techniques to determine flow rates through small areas of nanomaterials are desirable for such studies and in furthering our understanding of unique transport phenomena encountered at the nanoscale.[2,60–62] Molecular simulations and theoretical modelling have provided considerable insight into transport mechanisms through nanopores.[28,36,63–106] However, uncertainty in factors such as probable pore structures or intermolecular interaction potential leave a need for experimental data to corroborate such modelling.

Unfortunately, standard techniques for measuring fluid flows can be difficult to scale to micron and sub-micron sizes. Patch clamps are well established tools for sensitively measuring ion transport rates through small areas and have been successfully used in nanostructured membrane research.[20,22,107,108] Measuring uncharged species transport remains a major challenge, though some clever methods have been devised.[17,19,109–115] Bunch and collaborators[19,109,110] developed a technique to measure gas flow rates through micronscale areas of porous graphene by sealing a microcavity with the graphene, puncturing it by UV/ozone exposure, charging the cavity with gas in a pressure chamber, then subsequently measuring the inflation/deflation rate by atomic force

microscopy. Bocquet and collaborators[17,112] developed and applied two methods to measure liquid water flow rates out of single carbon and boron nitride nanotubes. Both methods use optical microscopy to image the larger-scale, slower flow in a downstream reservoir produced by a smaller, faster nanojet emerging from a pore too small to observe through an optical microscope. One approach was to use micro-particle image velocimetry to map the velocity field induced in a reservoir by flow out of a nanotube, then compare it to the analytical Landau-Squire[116,117] solution for the velocity field produced by a concentrated force in an infinite reservoir. The second approach was to inject dye through the capillary and use fluorescence microscopy to image the resulting plume, then compare it to an analytical solution for the concentration field of a solute in a Landau-Squire jet flow.

This study is motivated by the possibility of measuring volume flow rates through small membrane areas from microscope images of larger dye dispersions that form downstream. A prominent characteristic of membrane pores is the flat membrane surface that they extend through. This boundary is a distinct difference from the Landau-Squire jet geometry and requires a different flow field solution. For this geometry, Sampson[118] derived the velocity field in the low Reynolds number (creeping flow) limit. Atwal et al.[119] recently solved the advection-diffusion equation approximately for this flow field and developed a relation for the concentration field. In the high Reynolds number limit, Squire[120] and Yatseyev[121] derived an analytical similarity solution for flow emanating from a concentrated force directed away from a wall, though without satisfying the no-slip condition along the boundary.[122] Schneider[123,124] later approached this problem by dividing the flow into an inner jet and outer entrainment flow for the case of infinite Reynolds number. Recently, Gusarov[125] extended the analysis of Squire[120] and Yatseyev[121] to derive analytical equations for the velocity field enforcing the no-slip condition. Although this solution corresponds to zero-mass flux through the wall, Gusarov[126] validated the solution by comparing with numerical solutions for the flow field produced by a jet emerging through a hole in a wall.

In this paper, we seek to develop and validate a technique for determining volume flow rates of liquids through orifice plates in the laminar regime from images of dye dispersions downstream. We develop equations for the concentration field in the low and high Reynolds number limits based on existing analytical solutions for the flow field and compare images of fluorescent dye dispersion to these predictions. Although this work is motivated by flow through nanopores, to validate the technique and the Reynolds number range of validity of the analytical

solutions employed, we image fluorescent dye dispersions created downstream of micron-scale orifices, for which volume flow rates can be confidently calculated. In the low Reynolds number limit, we show that volume flow rate can be determined from the slope of concentration with inverse distance from the pore. We validate this approach with experimental plume images and find that it gives reasonable results up to a Reynolds number based on pore diameter of 15. At high Reynolds numbers, we develop an analytical similarity solution for the concentration field of a solute in Squire's[120] flow field solution. We similarly compute the concentration field numerically for Gusarov's[125] flow field solution. Comparing the dye dispersion images to computed streamlines and isoconcentration contours, we find good agreement for Reynolds numbers above 25.

This paper is organized as follows. Section II describes the dye dispersion experiments and flow rate calculations. Section III presents a selection of dye dispersion images and the governing equations for the concentration field. Section IV considers the low Reynolds number limit; the approximate solution for the concentration field is reviewed before applying it to show how volume flow rate can be extracted. This approach is validated by application to experimental plume images. Section V considers the high Reynolds number limit; similarity solutions for the flow field are reviewed and then corresponding similarity solutions to the advection-diffusion equation are derived for the concentration field. The results are compared to experimental images before a summary of the conclusions are presented in Section VI.

II. METHODS

Dispersions of fluorescent dye were produced by applying a pressure difference across a micropore in a transmission electron microscope (TEM) grid initially separating fluorescein upstream and water downstream (Fig. 1). The resulting flow was recorded on a fluorescence microscope to capture dispersion shapes and fluorescence intensity profiles.

A. Experimental methods

TEM grids, each with a single micropore in the center, formed the orifice plate geometry (Fig. 1a-d). Micropores of diameter 1, 3, and 6 μm (Norcada NTPR005A-C1, NTPR005D-C3, NTPR003D-C6) extend through a square silicon nitride window in a 3 mm diameter, 200 μm thick

silicon frame. The silicon nitride thickness is 50 nm for the 1 µm diameter pore and 200 nm for the 3 and 6 µm diameter pores. The pore diameter fabrication tolerance is ± 50 nm. Micropores of 50 µm diameter are punched through 3 mm diameter, 25 µm thick copper foil (SPI Supplies, 2885C-XA).

To promote wetting of the pore, the hydrophilicity of silicon TEM grids was increased by UV/ozone cleaning (Bioforce ProCleaner, 20 min) just before installing in the flow cell. To expose both sides, the grid was held vertically on Kapton polyimide tape (McMaster-Carr) during cleaning.

The flow cell was 3D printed (FormLabs Form3, GREY v4 resin), washed in isopropanol (IPA), and cured by ultraviolet light exposure (FormLabs FormCure, 30 min, 60^{o}C).

The TEM grid was mounted with Kapton polyimide tape over a 2 mm diameter opening between the upstream channel and downstream reservoir of the flow cell shown in Fig. 1e and sealed with JB Weld MarineWeld adhesive. A 1 mm thick microscope slide (25 mm $\times$ 75 mm) and 0.15 mm thick cover glass (22 mm $\times$ 40 mm) formed the bottom and top walls of the downstream reservoir, respectively, and were also attached using JB Weld MarineWeld adhesive. After assembly, the flow cell is left to dry for 1 h before charging with liquid.

Upstream of the pore, the flow cell was filled with a 1.5 mM solution of fluorescein dye (Millipore Sigma, F2456) in deionized (DI) water whereas the downstream reservoir was filled with DI water. Both fluids were passed through a 0.45 µm syringe filter and vacuum degassed for 2 h prior to charging the flow cell.

The upstream channel in the flow cell is 3 mm in diameter and follows a curved path between threaded inlet/outlet ports (Fig. 1e). The upstream channel is first filled by pipetting fluorescein dye into one of the upstream ports while angling the cell to force air out of the other port. Once the upstream side is filled, the inlet port is connected to a supply vial (Fig. 1f) containing fluorescein dye by 1.66 mm Idex PFA tubing (Cole Parmer) and an Idex flangeless fitting (Cole Parmer). The outlet port is closed with a second Idex flangeless fitting. The downstream reservoir is filled in the same way, closing the inlet port while connecting the outlet port to the waste vial (Fig. 1f). During the experiment, a pressure difference in the range 9 - 1000 mbar, with 0.5 mbar accuracy, is applied across the TEM grid using a pressure controller (Elveflow, MK1) connected to the supply and waste vials (Fig. 1f).

The flow cell is placed on the stage of a fluorecence microscope (Zeiss, AxioImager A2m) on an anti-vibration table. Top-down, reflected light images (Fig. 1g) were acquired using an X-Cite

Accepted to Phys. Fluids 10.1063/5.0142808

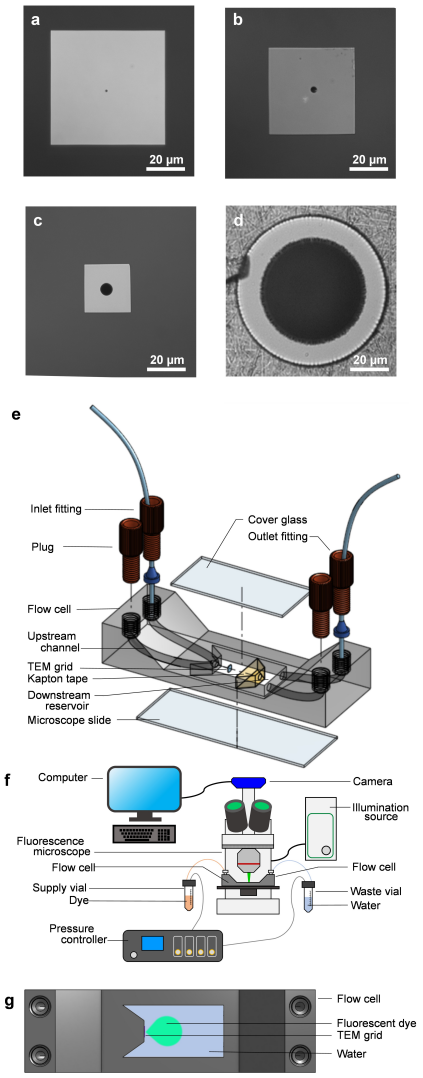

Figure 1: **Experimental setup. a-d** Micrographs of 1, 3, 6, and 50 µm pores, respectively. **e** Flow cell assembly. **f** Schematic showing layout of experiment and connections. **g** Top view of flow cell.

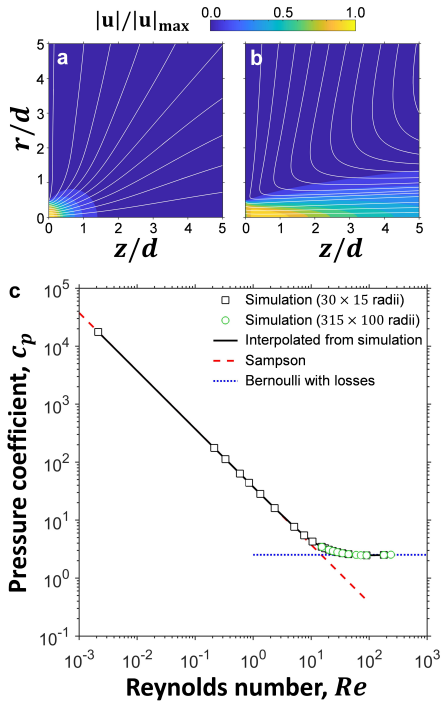

Figure 2: **Flow rate simulation results. a,b** Streamlines and flow speed color maps for (a) $Re = 0.002$ and (b) $Re = 44$. Here $|\mathbf{u}|$ is the magnitude of velocity and $|\mathbf{u}|_{\max}$ is the maximum magnitude of velocity in the flow. **c** Pressure coefficient dependence on Reynolds number for an infinitesimal thickness orifice plate.

XYLIS light emitting diode (LED) light source with a FITC filter cube (Zeiss, Filter Set 38 HE), a 5× objective lens (Zeiss, EC EPIPLAN 5×/0.13 HD), and a digital color camera (Zeiss, Axiocam 705, 5 MP).

B. Flow rate calculations

The flow rate from an infinitesimal thickness orifice plate varies with pore diameter and applied pressure difference. This dependence is expressed non-dimensionally as a dependence of pressure coefficient ($c_p = 2\Delta p/\rho V^2$) on Reynolds number ($Re = Vd/\nu$). Here, Δp is the pressure difference applied across the pate, d is the pore diameter, V is the average flow speed through the pore, ρ is density, and ν is kinematic viscosity. It is also common to express this

relation instead in terms of a discharge coefficient, also called an orifice coefficient, defined as $c_o = 1/\sqrt{c_p}$.[127,128]

At low Reynolds numbers ($Re << 1$), the average flow speed through the orifice plate is given by Sampson's[118] relation,

$$V = \frac{\Delta p\, d}{6\pi\mu}, \tag{1}$$

where $\mu = \rho\nu$ is the dynamic viscosity. Rearranging this relation in terms of the pressure coefficient gives,

$$c_p = \frac{12\pi}{Re}. \tag{2}$$

At high Reynolds numbers ($Re >> 1$), Bernoulli's equation corrected for losses[129] provides the appropriate scaling for flow rate, leading to,

$$c_p = K_L, \tag{3}$$

where K_L is the loss coefficient.

Neither equation accurately predicts flow rates at intermediate Reynolds numbers. Measurements and simulations have been performed on thin orifice plates (small plate thickness to diameter ratio), often inside larger diameter pipes, to determine this trend.[127,128,130–132] To obtain precise values for an infinitesimal thickness plate in a large reservoir, we perform computational fluid dynamics simulations of laminar, steady, incompressible, axisymmetric flow over a range of Reynolds numbers in OpenFOAM[133] (v2112, simpleFoam). We simulate a 1° slice of the cylindrical domain with a constant high pressure condition imposed on the upstream side of the plate at both the axial end and outer radial surface. A constant low pressure condition was similarly imposed on the downstream side of the plate at both the axial end and outer radial surface. Zero pressure gradient conditions were imposed along the plate and on the symmetry axis. Zero velocity gradient conditions were applied on the axial ends and outer radial surfaces and also on the symmetry axis. No-slip conditions were imposed on the plate surface.

Calculations were first performed on a uniform grid extending 15 pore radii upstream, downstream, and radially outward from the pore, using a grid spacing of 0.02 radii (designated 30×15 radii simulations). For $Re > 15$, we repeated these simulations on an expanding grid to simulate a farther distance downstream and verify that the effects of any jet development are accurately captured. This grid extends 300 pore radii downstream, 15 pore radii upstream, and

100 pore radii in the radial direction outward (designated 315×100 radii simulations). It has a uniform spacing of 0.02 radii in the radial direction over the pore, then expands with a constant cell-to-cell expansion ratio to 0.044 radii at the outer edge. In the axial direction, it expands with a constant cell-to-cell expansion ratio both upstream and downstream away from the pore, beginning with a value of 0.02 radii at the pore and expanding to a value of 0.50 radii at the downstream end.

Figure 2 shows examples of computed flow fields and the dependence of pressure coefficient on Reynolds number. It follows the predictions of Sampson's equation at low Reynolds numbers and approaches a constant value at high Reynolds numbers as predicted by the Bernoulli equation with losses. The simulations provide a value for loss coefficient of $K_L = 2.5$, within the range reported from prior studies on thin orifice plates.[127,128,130–132] The computed volume flow rates from the uniform and expanding grid simulations agree to within 1%. Flow rates for intermediate Reynolds numbers are obtained by interpolation from these simulation data.

The non-zero orifice plate thickness contributes to error in the computed volume flow rates. This error is included in uncertainty bars presented in later plots and is estimated by adding the orifice plate resistance in series with the Poiseuille flow expression for resistance in a fully developed laminar pipe flow. This approach was shown to provide flow rate predictions accurate to with 1% for non-zero thickness orifice plates in the low Reynolds number limit by Dagan et al.[134]

III. CONCENTRATION FIELDS

Figure 3 shows five examples of dye dispersion images taken with different pore diameters and applied pressures. Images are presented top to bottom in order of increasing Reynolds number. In these images, the TEM grid is located on the left side of the image. A pressure difference is applied, with higher pressure on the left side of the TEM grid and lower pressure on the right side. To the right of the TEM grid, the dye dispersion that forms downstream of the pore is observed.

The lower Reynolds number images (Fig. 3a,b) show approximately hemispherical plumes downstream of the pore, with the size of the plume increasing with Reynolds number. At intermediate Reynolds numbers (Fig. 3c), the plumes become elongated along the axis of the pore. At high Reynolds numbers (Fig. 3d,e), the dye dispersions develop into narrow jets, extending out of the field of view.

Accepted to Phys. Fluids 10.1063/5.0142808

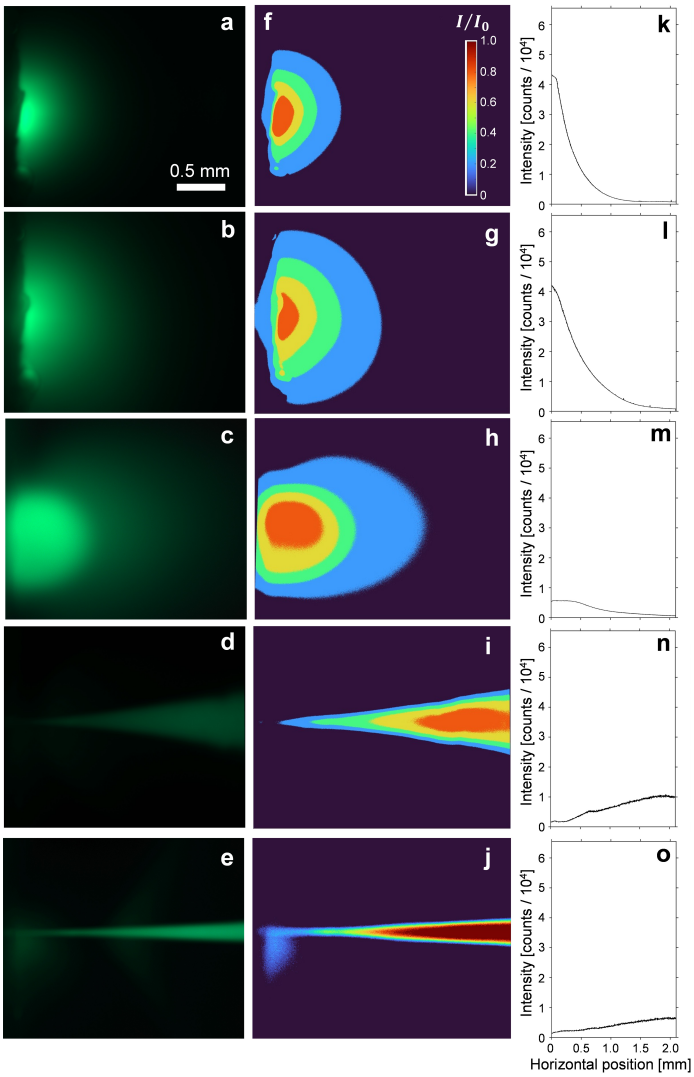

Figure 3: **Selected dye dispersion images. a-e** Photographs. **f-j** Processed intensity color maps. **k-o** Raw image intensity traces along a horizontal line passing through the pore, shown on the full 16 bit scale. Scale bar in (a) applies to panels (a)-(j). Intensity scale in (f) applies to panels (f)-(j). (a,f,k) $d = 1\,\mu\text{m}$, $\Delta p = 550$ mbar, $Re = 2.9$, (b,g,l) $d = 1\,\mu\text{m}$, $\Delta p = 950$ mbar, $Re = 4.8$, (c,h,m) $d = 6\,\mu\text{m}$, $\Delta p = 80$ mbar, $Re = 12$, (d,i,n) $d = 6\,\mu\text{m}$, $\Delta p = 200$ mbar, $Re = 22$, and (e,j,o) $d = 6\,\mu\text{m}$, $\Delta p = 250$ mbar, $Re = 25$.

The brightness intensity of each pixel in these images is related to the fluorescein concentration and can be used to analyse the concentration field downstream of the pore (Fig. 3f-o). By comparing the observed concentration field to analytical models for the concentration field, we seek to calculate the volume flow rate through the pore directly from dye dispersion images. To do this, we first examine analytical solutions for the concentration field downstream of the pore.

A. Governing equations for the concentration field

Laminar flow through a circular orifice is governed by the steady, incompressible, axisymmetric, zero swirl Navier-Stokes equations. In spherical coordinates, the continuity and momentum equations are,[135]

$$\frac{1}{R^2}\frac{\partial}{\partial R}\left(R^2 u_R\right) + \frac{1}{R\sin\theta}\frac{\partial}{\partial\theta}\left(u_\theta \sin\theta\right) = 0, \tag{4}$$

$$u_R\frac{\partial u_R}{\partial R} + \frac{u_\theta}{R}\frac{\partial u_R}{\partial\theta} - \frac{u_\theta^2}{R} = -\frac{1}{\rho}\frac{\partial p}{\partial R} + \nu\left[\frac{1}{R^2}\frac{\partial^2}{\partial R^2}\left(R^2 u_R\right) + \frac{1}{R^2\sin\theta}\frac{\partial}{\partial\theta}\left(\sin\theta\frac{\partial u_R}{\partial\theta}\right)\right], \tag{5}$$

$$u_R\frac{\partial u_\theta}{\partial R} + \frac{u_\theta}{R}\frac{\partial u_\theta}{\partial\theta} + \frac{u_R u_\theta}{R} = -\frac{1}{\rho R}\frac{\partial p}{\partial\theta} + \nu\left[\frac{1}{R^2}\frac{\partial}{\partial R}\left(R^2\frac{\partial u_\theta}{\partial R}\right) + \frac{1}{R^2}\frac{\partial}{\partial\theta}\left(\frac{1}{\sin\theta}\frac{\partial}{\partial\theta}\left(u_\theta\sin\theta\right)\right) + \frac{2}{R^2}\frac{\partial u_R}{\partial\theta}\right], \tag{6}$$

where u_R and u_θ are the R and θ components of velocity in spherical coordinates and p is pressure. For a dilute dye, the concentration field is governed by the steady advection-diffusion equation, which in spherical coordinates is,[135]

$$u_R\frac{\partial C}{\partial R} + \frac{u_\theta}{R}\frac{\partial C}{\partial\theta} = D\left[\frac{1}{R^2}\frac{\partial}{\partial R}\left(R^2\frac{\partial C}{\partial R}\right) + \frac{1}{R^2\sin\theta}\frac{\partial}{\partial\theta}\left(\sin\theta\frac{\partial C}{\partial\theta}\right)\right], \tag{7}$$

where C is concentration and D is the mass diffusion coefficient of the dye.

A general solution for the flow field over all laminar Reynolds numbers is not available, however, solutions do exist for the low and high Reynolds number limits.[118,120,125] We consider these two cases separately in the following sections.

Accepted to Phys. Fluids 10.1063/5.0142808

IV. LOW REYNOLDS NUMBER PLUMES

In the low Reynolds number limit, the left hand sides of Eq. 5 and 6 are negligible, reducing Eq. 4-6 to Stokes equations. Sampson[118] solved these equations analytically for pressure driven flow through a circular hole in a zero-thickness wall in an unbounded domain and obtained the velocity field,

$$u_r = \frac{3}{2} V \frac{q^2 s}{s^2+q^2}\sqrt{\frac{1-q^2}{1+s^2}}, \qquad u_z = \frac{3}{2} V \frac{q^3}{s^2+q^2}, \tag{8}$$

where q and s are non-dimensional oblate-spheroidal coordinates, defined with respect to axisymmetric cylindrical coordinates by $r = \frac{1}{2} d\sqrt{(1+s^2)\,(1-q^2)}$ and $z = \frac{1}{2} dqs$. Here V is the average flow speed through the hole given by Eq. 1, z is the axial distance measured from the center of the hole, r is the radial distance measured from the z axis, and u_r and u_z are the r and z components of velocity.

The advection-diffusion equation (Eq. 7) in oblate-spheroidal coordinates for this velocity field is,[119,136]

$$\frac{3}{4} Pe\, q^2 \frac{\partial c}{\partial s} = \frac{\partial}{\partial s}\left[\left(1+s^2\right)\frac{\partial c}{\partial s}\right] + \frac{\partial}{\partial q}\left[\left(1-q^2\right)\frac{\partial c}{\partial q}\right], \tag{9}$$

where $c = C/\Delta C$ is the non-dimensional concentration, ΔC is the concentration difference between far upstream and far downstream of the hole, and $Pe = Vd/D$ is the Péclet number.

We consider the case of zero dye concentration far from the hole on the downstream side, expressed by the boundary condition $c(q, s \to \infty) = 0$. The condition of uniform concentration far from the hole on the upstream side is $c(q, s \to -\infty) = 1$. Furthermore, the impermeability of the wall requires $\left.\frac{\partial c}{\partial q}\right|_{q=0} = 0$.

Atwal et al.[119] applied a Legendre polynomial integral transform to convert the partial differential equation in Eq. 9 into an equivalent system of ordinary differential equations given by,

$$\frac{3}{4} Pe \left[\frac{n^2+3n+2}{4n^2+8n+3}\frac{d\hat{c}_{n+2}}{ds} + \frac{2n^2+2n-1}{4n^2+4n-3}\frac{d\hat{c}_n}{ds} + \frac{n^2-n}{4n^2-1}\frac{d\hat{c}_{n-2}}{ds}\right] = \frac{d}{ds}\left[\left(1+s^2\right)\frac{d\hat{c}_n}{ds}\right] - n\,(n+1)\,\hat{c}_n(s), \tag{10}$$

where the concentration field is expanded in the form,

$$c(q,s) = \sum_{n=0,2,4,\ldots}^{\infty} \frac{2n+1}{2}\,\hat{c}_n(s)\,P_n(q), \tag{11}$$

with $P_n(q)$ being the n^{th} degree Legendre polynomial, normalized such that $\int_0^1 P_n(q)\,P_m(q)\,dq = \frac{1}{2n+1}\delta_{m,n}$.[137] Here, $\delta_{m,n}$ is the Kronecker delta and $\hat{c}_n(s)$ are the integral transform coefficient functions. We define $\hat{c}_{-2}(s) = 0$ to avoid treating the $n = 0$ case separately.

Eq. 11 enforces the wall impermeability boundary condition by excluding terms with odd values of n. The concentration boundary conditions far from the hole become, $\hat{c}_n(s \to -\infty) = 2\delta_{0,n}$ and $\hat{c}_n(s \to \infty) = 0$.

This system of equations can be solved numerically by truncating the concentration field expansion (Eq. 11) at a finite value of n. Often, high accuracy solutions can be obtained with a small number of terms using integral transform formulations.[138] Example concentration fields from numerical solutions to Eq. 10 and boundary conditions are presented for various values of Pe in Fig. 4a-d. These calculations were performed with the series truncated to the $n = 20$ term with 200,001 equally spaced grid points over the domain, using a fourth order finite difference discretization at interior grid points and second order finite difference discretization at the boundaries. To avoid truncating the infinite domain when solving Eq. 10 numerically, the equations are first mapped to a finite domain, as described in Ref. 119.

A. Leading order solution for the concentration field

Atwal et al.[119] also found that truncating the concentration series expansion to a single term provides an analytical expression for the solute mass flux through the hole that correctly predicts the solute mass transfer rate to within 1%. Retaining only the $n = 0$ term in Eq. 10 leads to,

$$\frac{Pe}{4}\frac{d\hat{c}_0}{ds} = \frac{d}{ds}\left[\left(1+s^2\right)\frac{d\hat{c}_0}{ds}\right], \tag{12}$$

with boundary conditions $\hat{c}_0(s \to -\infty) = 2$ and $\hat{c}_0(s \to \infty) = 0$. Solving this equation for $\hat{c}_0$ and substituting back into Eq. 11 results in an approximation for the concentration field of,

$$c(q,s) = \frac{\exp\left(\frac{Pe}{4}\arctan s\right) - \exp\left(\frac{\pi Pe}{8}\right)}{\exp\left(-\frac{\pi Pe}{8}\right) - \exp\left(\frac{\pi Pe}{8}\right)}. \tag{13}$$

We propose to use the rate of decay of concentration with distance from the pore along the z axis in the downstream reservoir as a way to measure the flow rate through the pore. Along the

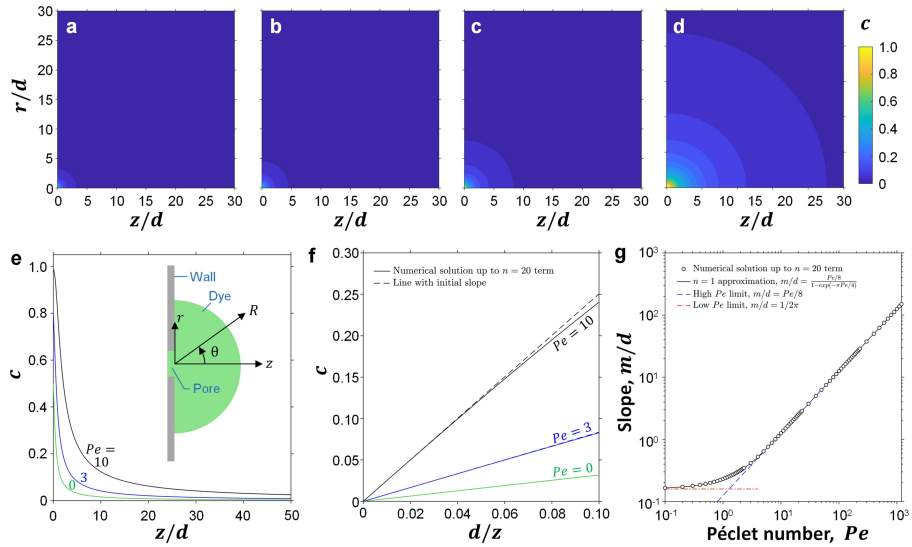

Figure 4: **Solution for low Reynolds number concentration field. a-d** Color maps of concentration field from numerical solution up to $n = 20$ term for (a) $Pe = 0$, (b) $Pe = 1$, (c) $Pe = 3$, and (d) $Pe = 10$. **e** Example concentration profiles along the z-axis. Inset is a sketch of the plume with coordinate definitions. **f** Example concentration profiles plotted with respect to inverse distance from the pore. **g** Far field slope characterizing concentration decay from the numerical solution up to $n = 20$ term compared to approximate relations.

z axis ($q = 1$), $s = 2z/d$. Far from the pore ($s >> 1$), this means that $\arctan s \approx \pi/2 - d/2z$, and Eq. 13 simplifies to,

$$c \approx \frac{1 - \exp\left(\dfrac{-Ped}{8z}\right)}{1 - \exp\left(\dfrac{-\pi Pe}{4}\right)}, \tag{14}$$

which reveals the rate of decay of concentration with distance from the pore. Example curves illustrating this concentration decay are presented in Fig. 4e,f. We define the distant decay rate, m, as the slope of c vs. $1/z$ far from the pore, *i.e.*,

$$m = \left.\frac{dc}{d\left(\frac{1}{z}\right)}\right|_{z\to\infty}. \tag{15}$$

Evaluating m (Eq. 15) for the leading order solution at low Reynolds number (Eq. 14) gives a

decay rate of,

$$m = \frac{\frac{Ped}{8}}{1 - \exp\left(\frac{-\pi Pe}{4}\right)}. \tag{16}$$

For $Pe << 1$, this becomes $m = d/2\pi$ whereas for $Pe >> 1$ it becomes $m = Ped/8$. Eq. 16 along with the low and high Pe limits are compared to the full numerical solution for the low Reynolds number concentration field in Fig. 4g. Eq. 16 is accurate to within 1% for the points shown. For $Pe > 7$, the equation for the high Pe limit is also accurate to within 1%.

Substituting the definition of Pe into the high Péclet number limit of Eq. 16 predicts a decay rate of,

$$m = \frac{Q}{2\pi D}, \tag{17}$$

where $Q = V\pi d^2/4$ is the volume flow rate through the pore. By measuring the slope of c vs. $1/z$ at large z, Eq. 17 can be used to determine the volume flow rate through the hole. Conveniently, Eq. 17 can be used to determine the volume flow rate from the concentration field without knowledge of the hole diameter, provided Re is small and Pe is large.

B. Similarity solution for the low Reynolds number flow field

Gusarov[126] derived a similarity solution for the velocity field in a semi-infinite reservoir created by flow into the reservoir from a small hole in a wall at low Reynolds number. He found a solution for the flow field of the form,

$$u_R = \frac{\phi(\theta)}{R^2}, \quad u_\theta = \frac{f(\theta)}{R^2}, \quad \frac{p}{\rho} = \frac{g(\theta)}{R^3}, \tag{18}$$

by substituting these expressions into the Navier-Stokes equations (Eq. 4-6) with the terms on the left of Eq. 5 and 6 set to zero. This leads to,

$$\frac{1}{\sin\theta}\frac{d}{d\theta}\left(\frac{d\phi}{d\theta}\sin\theta\right) + \frac{3g}{\nu} = 0, \quad \frac{1}{\nu}\frac{dg}{d\theta} = 2\frac{d\phi}{d\theta} + 2f, \quad \frac{d}{d\theta}\left(f\sin\theta\right) = 0. \tag{19}$$

Including the impermeable wall condition that $f(\theta = \pi/2) = 0$ for $R > 0$ (*i.e.*, assuming the hole is infinitesimally small) and no-slip condition that $\phi(\theta = \pi/2) = 0$, Eq. 19 is solved resulting in

$f(\theta) = 0$ and

$$\phi(\theta) = A\left[\left(3\cos^2\theta - 1\right)\ln\left(\frac{1+\cos\theta}{1-\cos\theta}\right) - 6\cos\theta\right] - B\cos^2\theta, \tag{20}$$

where A and B are integration constants. Eq. 20 gives the θ dependence of u_R. The first term on the right is singular at $\theta = 0$. Gusarov[126] found that including only the second term on the right (*i.e.*, choosing $A = 0$) provided good agreement with numerical solutions for the flow field at $Re \lesssim 10$. This corresponds to a velocity field of

$$u_\theta = 0 \quad \text{and} \quad \mathrm{u_R} \propto \frac{\cos^2\theta}{\mathrm{R}^2}. \tag{21}$$

We note that this velocity field scaling matches that of Sampson's[118] solution (Eq. 8) at large distances from the hole. This can be shown by noting that since $0 \leq q \leq 1$, at $R >> d$, $s >> 1$ and $R \approx \frac{1}{2}ds$. Furthermore, for Sampson's[118] velocity field (Eq. 8) at $s >> 1$, $\tan\theta = r/z \approx \sqrt{1-q^2}/q \approx u_r/u_z$. This shows that $\cos\theta \approx q$, $\sin\theta \approx \sqrt{1-q^2}$, $u_\theta \approx 0$, and $u_R \approx \sqrt{u_r^2 + u_z^2}$. Using these approximations and Sampson's[118] velocity field (Eq. 8) in this last expression for u_R leads to Eq. 21, verifying that Sampson's[118] and Gusarov's[126] solutions give the same scaling far from the pore. Therefore, Gusarov's[126] similarity solution for the concentration field at low Reynolds numbers leads to the same prediction for the rate of decay of the concentration field as obtained from Sampson's[118] solution for the flow field far from the hole (Eq. 16 and 17). Furthermore, although derived for $Re << 1$, since Gusarov[126] found good agreement between numerical solutions and this flow field even in the range $2 \lesssim Re \lesssim 10$, we expect to be able to apply this approach for $Re \sim 1$

C. Measuring flow rate from concentration field images

We propose to measure the rate of decay of concentration with distance from the pore from images of fluorescent plumes to determine the volume flow rate. Images taken with different pore diameters and applied pressures were acquired with different illumination intensities and exposure times to provide high contrast without overexposure in regions where measurements are made. Pixel intensity values were scaled down by the fluorescence intensity and exposure time to translate intensity values in each image onto the same relative scale.

Measured intensity profiles (Fig. 5a) are plotted with respect to $1/z$ (Fig. 5b) and the

Accepted to Phys. Fluids 10.1063/5.0142808

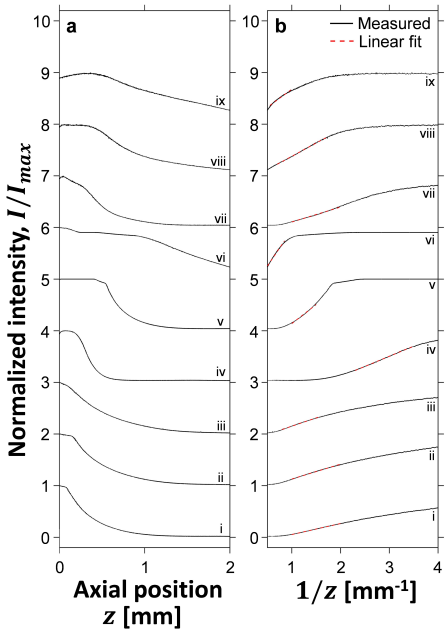

Figure 5: Measured light intensity (I) profiles, normalized by the maximum intensity within the image ($I_{\max}$), plotted against **a** axial distance from the pore (z) and **b** inverse axial distance from the pore ($1/z$). Each profile is offset vertically from the previous profile by 1. The diameter and pressure difference for the profiles are: (i) $1\,\mu$m, 550 mbar, (ii) $1\,\mu$m, 750 mbar, (iii) $1\,\mu$m, 950 mbar, (iv) $3\,\mu$m, 100 mbar, (v) $3\,\mu$m, 200 mbar, (vi) $3\,\mu$m, 500 mbar, (vii) $6\,\mu$m, 41 mbar, (viii) $6\,\mu$m, 80 mbar, (ix) $6\,\mu$m, 130 mbar.

slope is calculated by least squares fitting over the linear range. The resulting slope should be proportional to volume flow rate according to Eq. 17. All measurements are performed with the same dye and at the same upstream concentration. Thus, a single scaling factor common to all measurements taken on the system can be applied to map the measured slope to volume flow rate. Once this calibration factor is determined for one pore, it can be applied to measurements for all pores.

Here, we find the calibration factor by least squares fitting the measured slopes to the calculated volume flow rates for the full set of measurements (Fig. 6a). The ability of this single calibration factor to provide close agreement of the measured volume flow rates to the calculated values in Fig. 6a provides validation for the method.

The same results are shown in non-dimensional form in Fig. 6b. From this it is seen that accurate results can be obtained up to a Reynolds number of ~ 15. However, it should be noted that the dye plumes start to become elongated in the axial direction at the higher end of this range. This results in greater uncertainty in the measurement, as reflected in the errorbars in Fig. 6b, due to greater variation in the measured slope with the axial location where it is taken. Other potential sources of error in this method include background fluorescence noise created by slow dye accumulation in the far field over time due to the finite reservoir size and contributions from out-of-focal plane dye particles on the recorded fluorescence intensity.[139] If applied to very low flow rates, the impacts of photobleaching due to long residence times in the field of view would have to be examined and alternative fluorophores may perform better. The need for optical access to the downstream reservoir and susceptibility to blockage by dye particle agglomerations are also considerations when employing this approach.

We further note that because the method developed here only relies on image intensity data far from the pore, it can be applied even if images are overexposed in regions near the pore, where the dye concentration is high. In some cases, allowing such overexposure may make better use of the image sensor range in regions far from the pore where the measurement is made.

D. Control volume approximation for $Re \sim 1$

By comparison with numerical solutions, Gusarov[126] found that his similarity solution for the velocity field (Eq. 21) far from a pore derived for $Re << 1$ was actually accurate up to $Re \approx 10$. Consistent with this finding, we observe from experiment that although Eq. 17, relating the rate of decay of concentration to the volume flow rate, was derived in the $Re << 1$ limit, it provides reasonable values for flow rate at Reynolds numbers even up to $Re \approx 15$. We rationalize this result in the case of concentration based on the observation that there is a small Reynolds number range ($10 \lesssim Re \lesssim 20$) between the dye dispersion being approximately hemispherical and the formation of a narrow jet. Even though Sampson's[118] solution for the flow field at $Re << 1$ will not apply up to $Re \approx 15$, the lack of a narrow jet means that the flow speed will decrease rapidly with radius in all directions at these Reynolds numbers. While strong advection is primarily responsible for solute being carried through the orifice, many diameters from the pore, transport will be primarily by diffusion (Fig. 7).

With this approximate model for mass transfer in mind, we consider steady solute mass

Accepted to Phys. Fluids 10.1063/5.0142808

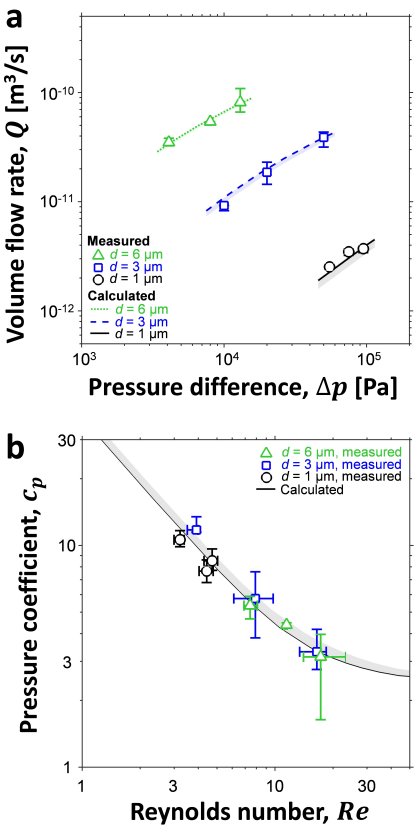

Figure 6: **Comparison of measured flow rates to computed flow rates. a** Volume flow rate vs applied pressure difference for pores of three different diameters. Error bars on measurements include standard error in least squares fit for the calibration factor and also minimum and maximum difference in computed intensity slope for $\pm 15\%$ shift in the $1/z$ range where the linear fit is performed. Shaded areas show uncertainty in calculated curves due to fabrication tolerance on pore diameter and the non-zero thickness of the orifice plate. **b** Pressure coefficient vs Reynolds number. Error bars on measurements include uncertainty in volume flow rate included in panel (a) as well as fabrication tolerance in diameter. Shaded area shows uncertainty in calculated curve due to non-zero thickness of pores.

transfer in a one-dimensional hemispherical control volume with solute mass transfer through the pore being purely by advection, and that many diameters away from the pore being purely by diffusion (Fig. 7). The rate of mass advection through the pore is $\dot{m}_{\text{in}} = Q\Delta C$, where ΔC

Accepted to Phys. Fluids 10.1063/5.0142808

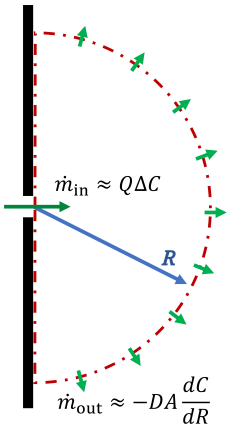

Figure 7: **Sketch of hemispherical control volume used in approximate one-dimensional control volume analysis.**

is the solute concentration far upstream of the orifice in this case, because the concentration far downstream is zero. The rate of mass diffusion away from the pore, far downstream of the pore, is $\dot{m}_{\text{out}} = -DA\frac{dC}{dR}$, where A is the area of the outflow control surface (*i.e.*, $A = 2\pi R^2$). Equating the rates of mass inflow and outflow results in the differential equation,

$$Q\Delta C = -2\pi R^2 D\frac{dC}{dR}. \tag{22}$$

Solving this equation with the boundary condition of zero concentration far downstream of the orifice (*i.e.*, $C(R \to \infty) = 0$) leads to a non-dimensional concentration of,

$$c = \frac{Q}{2\pi RD}. \tag{23}$$

Calculating the decay rate for this approximate concentration field by substituting Eq. 23 into Eq. 15 with $R = z$ results in,

$$m = \frac{Q}{2\pi D}, \tag{24}$$

the same as obtained in Eq. 17 from Sampson's[118] $Re << 1$ flow field.

This approximate analysis shows why, even through the precise flow field is not known analytically for higher Reynolds numbers in the range $Re \lesssim 15$, Eq. 17 can still be applied to calculate the flow rate from the rate of decay of concentration; in this Reynolds number range,

the flow speed decays sufficiently by the radius where the decay rate is measured that this rate is governed solely by diffusion, independent of the precise velocity field. This approximate control volume analysis does not assume a pore geometry in the membrane through which solute passes, only that it is through a small area relative to the size of the wall and distance at which the slope is measured. This implies that the same scaling and measurement approach will apply for pores of different geometries or even to flow through several parallel pores, such as in small areas of membrane materials. It further explains how similar $C \propto 1/R$ far field scaling is found both here for plumes emerging into semi-infinite reservoirs and also for Landau-Squire plumes[112] in infinite reservoirs. However, increasing the Reynolds number to the point that a jet forms invalidates the requirement of low flow speed at the radius where the slope is measured, as there will be a narrow region far from the orifice where the velocity is still high and advection remains important.

V. HIGH REYNOLDS NUMBER JETS

At $Re \gtrsim 20$, the dye dispersions abruptly transition into jets (Fig. 3) and the approach taken to measure flow rates from the decay of concentration used at lower Reynolds numbers cannot be applied. At these higher Reynolds numbers, we consider the possibility of comparing the dye dispersion to analytical solutions for laminar jet flow out of a wall.

A. High Reynolds number flow field

Similarity solutions for laminar jets issuing from a hole in a wall were derived by Squire[116,120], without satisfying the no-slip condition at the wall, and later by Gusarov[125,126], including the no-slip condition at the wall. Below, we first review the derivation of both of these velocity fields and then use them to develop an expression for the resulting concentration field for a solute flowing from the hole.

In both cases, a flow field of the form,

$$u_R = \frac{\phi(\theta)}{R}, \qquad u_\theta = \frac{f(\theta)}{R}, \qquad \frac{p}{\rho} = \frac{g(\theta)}{R^2}, \tag{25}$$

was shown to satisfy the Navier-Stokes equations by substituting these relations into Eqs. 4-6.

The resulting differential equations for ϕ, f, and g are,

$$\phi = -\frac{1}{\sin\theta}\frac{d}{d\theta}\left(f\sin\theta\right), \tag{26}$$

$$f\frac{df}{d\theta} + \frac{dg}{d\theta} = \nu\frac{d\phi}{d\theta} \tag{27}$$

$$f\frac{d\phi}{d\theta} - f^2 - \phi^2 - 2g = \frac{\nu}{\sin\theta}\frac{d}{d\theta}\left(\frac{d\phi}{d\theta}\sin\theta\right) \tag{28}$$

Eqs. 26-28 can be combined to eliminate g and ϕ, leaving a single differential equation for f,

$$\frac{df}{d\theta} = \frac{1}{2\nu}f^2 + f\cot\theta + 2\nu\left(\frac{a_2\cos\theta - a_1}{\sin^2\theta} + \frac{a}{2}\right), \tag{29}$$

where a, a_1, and a_2 are integration constants.

Squire[120] found that $a = a_1 = a_2$ corresponds to a jet flow from a hole in a wall, with velocity slip at the wall. For this case, the solution to Eq. 29 subject to the impermeable wall condition ($f(\theta = \pi/2) = 0$) is,[120]

$$\frac{f}{\nu} = \frac{2a\left(1-\cos\theta\right)}{\sin\theta\left[\sqrt{-1-2a}\cot\left(\frac{\sqrt{-1-2a}}{2}\ln\left(1+\cos\theta\right)\right) - 1\right]}. \tag{30}$$

One problem with this solution is that the total mass flow rate through a hemispherical shell centered on the hole varies with radius. Squire[116] proposed that such flows could instead be characterized by the equivalent force exerted at the origin that would produce this flow. It is calculated by integrating the z momentum transfer across a hemispherical shell, which for this flow is,[117,125]

$$M = 2\pi\rho\int_0^{\pi/2}\left[\left(u_R u_R + \frac{p}{\rho} - 2\nu\frac{\partial u_R}{\partial R}\right)\cos\theta - \left(u_R u_\theta - \nu\frac{1}{R}\frac{\partial u_R}{\partial\theta} - \nu\frac{\partial u_\theta}{\partial R} + \nu\frac{u_\theta}{R}\right)\sin\theta\right]R^2\sin\theta d\theta. \tag{31}$$

Different choices of a correspond to different values of M (Fig. 8a). At high Reynolds numbers, the first term on the right dominates and the rate of momentum transfer can be approximated as,

$$M_{approx} = 2\pi\rho\int_0^{\pi/2} u_R u_R R^2\cos\theta\sin\theta d\theta. \tag{32}$$

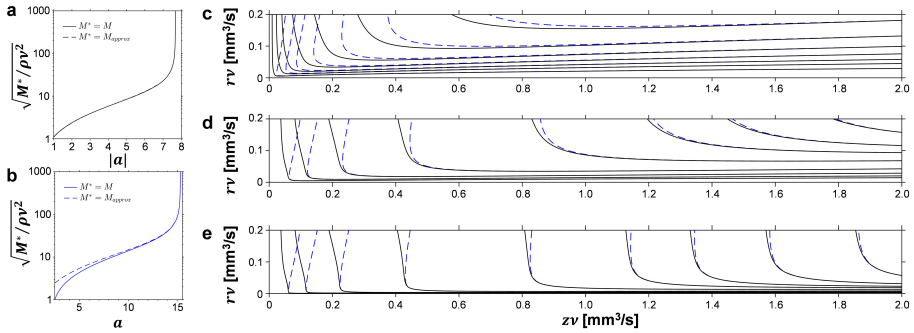

Figure 8: **High Reynolds number flow field solution. a,b** Applied force, M, computed as a function of the free parameter in the solution of (a) Squire[120] and (b) Gusarov.[125] **c-d** Example streamlines from Squire[120] (solid lines) and Gusarov[125] (dashed lines) solutions for (c) $\sqrt{M/\rho\nu^2} = 50$, (d) $\sqrt{M/\rho\nu^2} = 200$, and (e) $\sqrt{M/\rho\nu^2} = 1000$.

Gusarov[125,126] showed that, instead choosing $a = 2a_1 = 2a_2$, is necessary for both a finite value of momentum flux (M) and no-slip at the wall ($\phi(\theta = \pi/2) = 0$). He solved Eq. 29 and obtained,

$$\begin{aligned}\frac{f}{\nu} =& \left\{ 2\frac{\alpha\beta}{\gamma}\left(\cos\frac{\theta}{2}\right)^{\gamma+1}\sin^2\frac{\theta}{2}F\left(\alpha+1,\beta+1;\gamma+1;\cos^2\frac{\theta}{2}\right)\right. \\ &-\left(\cos\frac{\theta}{2}\right)^{\gamma-1}\left[2-(2+\gamma)\sin^2\frac{\theta}{2}\right]F\left(\alpha,\beta;\gamma;\cos^2\frac{\theta}{2}\right) \\ &+2b\frac{(2-\alpha)(2-\beta)}{2-\gamma}\left(\cos\frac{\theta}{2}\right)^{3-\gamma}\sin^2\frac{\theta}{2}F\left(3-\alpha,3-\beta;3-\gamma;\cos^2\frac{\theta}{2}\right) \\ &\left.-b\left(\cos\frac{\theta}{2}\right)^{1-\gamma}\left[2-(4-\gamma)\sin^2\frac{\theta}{2}\right]F\left(2-\alpha,2-\beta;2-\gamma;\cos^2\frac{\theta}{2}\right)\right\}\Bigg/ \\ &\left\{\left(\cos\frac{\theta}{2}\right)^{\gamma}\sin\frac{\theta}{2}F\left(\alpha,\beta;\gamma;\cos^2\frac{\theta}{2}\right)\right. \\ &\left.+b\left(\cos\frac{\theta}{2}\right)^{2-\gamma}\sin\frac{\theta}{2}F\left(2-\alpha,2-\beta;2-\gamma;\cos^2\frac{\theta}{2}\right)\right\},\end{aligned} \tag{33}$$

where F is the hypergeometric function, $2\alpha = 2 - \sqrt{1+a} + \sqrt{1+2a}$, $2\beta = 2 - \sqrt{1+a} - \sqrt{1+2a}$, and $\gamma = 1 - \sqrt{1+a}$. The constant b is calculated for a given value of a by enforcing the wall impermeability condition, that $f(\pi/2) = 0$. Different values of a correspond to different values of M (Fig. 8b). ϕ and g can be derived from the solution for f,[125] but this is not described

here because they are not needed in the concentration field derivation.

Both Squire's[120] and Gusarov's[125] solutions predict streamlines as curves of constant $fR\sin\theta$. Example streamlines are shown in Fig. 8c-e. Streamlines from the two solutions line up well along the jet axis far from the hole, with agreement improving at larger M. The solutions differ significantly near the wall, where one satisfies the no-slip condition whereas the other does not.

Unfortunately, neither Squire's[120] nor Gusarov's[125] solutions correspond to a jet with a constant, non-zero mass flow rate. However, by comparison to numerical solutions, Gusarov[126] did find reasonable agreement with streamlines produced by flow through a hole at high Reynolds numbers ($Re \gtrsim 30$). He further reasoned that the equivalent force parameter, $M/\rho\nu^2$, was proportional to Re^2, providing a parameter that can approximately relate the two flows. Setting $Re \approx \sqrt{M/\rho\nu^2}$ appears to be a reasonable approximation with Reynolds number defined based on average velocity through the hole and the hole diameter; $\sqrt{M_{approx}/\rho\nu^2}$ is within 6% of Re for both a parabolic velocity profile (corresponding to Poiseuille flow) and a semi-elliptical velocity profile (corresponding to Sampson[118] flow). Values of M as a function of a are provided in Fig. 8a,b and show that for $\sqrt{M/\rho\nu^2} > 20$, $\sqrt{M_{approx}}$ is within 4% of $\sqrt{M}$ for Gusarov's[125] flow field and within 1% for Squire's[120] flow field.

B. High Reynolds number concentration field

We consider the possibility of using the dispersion pattern of dye in the jet flow to estimate Re. Using either Squire's[120] or Gusarov's[125] solution for the jet flow field, an expression for the concentration field of a solute flowing with the jet can be derived. Substituting a concentration of the form,

$$C(R,\theta) = \frac{W(\theta)}{R}, \tag{34}$$

and the general form for the flow field (Eq. 25) into the advection diffusion equation (Eq. 7) leads to,

$$\frac{1}{\sin\theta}\frac{d}{d\theta}\left(\sin\theta\frac{dW}{d\theta}\right) = \frac{1}{D}\left[f\frac{dW}{d\theta} - \phi W\right], \tag{35}$$

where $W(\theta)$ is a function to be determined. Invoking Eq. 26 relating ϕ to f results in,

$$\frac{d}{d\theta}\left(\sin\theta\frac{dW}{d\theta}\right) = \frac{1}{D}\left[f\sin\theta\frac{dW}{d\theta} + W\frac{d}{d\theta}\left(f\sin\theta\right)\right]. \tag{36}$$

Factoring by reverse product rule and integrating gives,

$$\frac{dW}{d\theta} = \frac{1}{D} W f, \tag{37}$$

where the constant of integration has been set to zero to enforce the impermeability condition at the wall, *i.e.*,

$$\left.\frac{\partial C}{\partial \theta}\right|_{\theta=\frac{\pi}{2}} = 0, \tag{38}$$

or equivalently,

$$\left.\frac{dW}{d\theta}\right|_{\theta=\frac{\pi}{2}} = 0, \tag{39}$$

and the impermeable wall condition ($f\left(\pi/2\right) = 0$). Integrating again yields,

$$W = W_0 \exp\left(-Sc \int_{\theta}^{\pi/2} \frac{f(\theta')}{\nu} d\theta'\right), \tag{40}$$

where $Sc = \nu/D$ is the Schmidt number and W_0 is a constant. The integral in Eq. 40 can be evaluated for f from either Squire's[120] solution (Eq. 30) or Gusarov's[125] solution (Eq. 33). In the case of Squire's[120] solution, the integral is evaluated analytically by substituting Eq. 30 into Eq. 40, resulting in,

$$W = W_0 \left(\frac{(-1-2a)\left\{\cot^2\left[\frac{1}{2}\sqrt{-1-2a}\ln\left(1+\cos\theta\right)\right]+1\right\}}{(1+\cos\theta)\left\{\sqrt{-1-2a}\cot\left[\frac{1}{2}\sqrt{-1-2a}\ln\left(1+\cos\theta\right)\right]-1\right\}^2}\right)^{Sc}. \tag{41}$$

We evaluate Eq. 40 numerically for Gusarov's[125] solution.

Constant concentration contours have the shape $R \propto W(\theta)$. Example contours are presented in Fig. 9. At $Sc = 1$ (Fig. 9a), varying Re between 1 and 100 results in dye dispersions ranging from approximately hemispherical, as expected at low Reynolds numbers, to being highly elongated, as expected for high Re jets. Although these curves appear qualitatively reasonable, at $Re \lesssim 30$ the jet flow solutions are not valid[126] so these contours will not reflect the actual flow. At $Re = 1$ for example, the flow rate is accurately predicted by Sampson's[118] equation (Fig. 2c) where flow from the hole spreads in all directions (Fig. 2a) rather than forming a focused jet. This issue becomes more clear when considering the higher Schmidt number of ∼2500 for the fluorescein dye used in our experiments (Fig. 9b).[140] In this case, even for $Re = 1$,

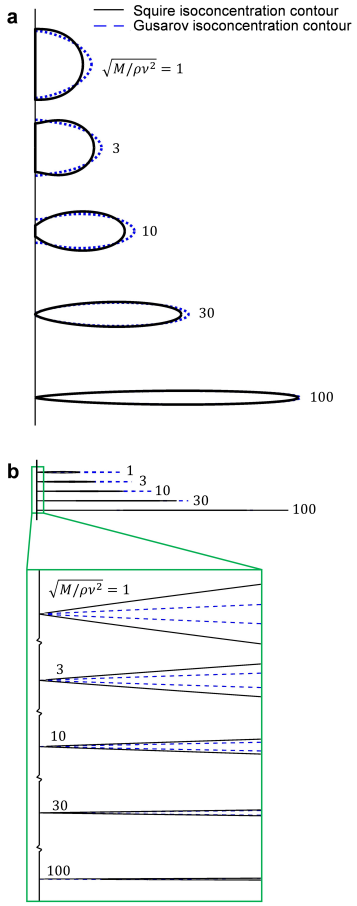

Figure 9: **High Reynolds number concentration field solution isoconcentration contour shapes.** Example isoconcentration contours are shown for various values of $\sqrt{M/\rho\nu^2}$ at **a** $Sc = 1$ and **b** $Sc = 2500$. The vertical and horizontal scales are one to one. Note that some values of $\sqrt{M/\rho\nu^2}$ plotted are below the expected range of validity of the high Reynolds number solutions.

the high Reynolds number concentration field solution produces extremely elongated jets.

Very near the pore, constant concentration contours appear to be approximately linear, in agreement with the jet images in Fig. 3. Although not apparent in Fig. 9b, very near the pore the concentration contours curve steeply as the pore is approached. As a result of this curvature, the

slope of the concentration contour near the pore depends strongly on which isoconcentration value is plotted. This value depends on W_0 and is not explicitly specified in Eq. 40. Instead, the curves in Fig. 9 are all normalized to have the same enclosed area. Consequently, the Squire and Gusarov isoconcentration contours in Fig. 9b have different slope near the pore, but this is not an indication of similarity or discrepancy between the two, as a different choice of normalization could be made to closely match these slopes.

A more reliable comparison of the Squire and Gusarov concentration fields is made based on isoconcentration contour shape in Fig. 10, by plotting the ratio of the contour widths (w_2/w_1) taken at two distances from the pore, the second twice as far as the first ($z_2 = 2z_1$). These distances are indicated in Fig. 10a. Figure 10b compares these ratios along contours of different M. All curves in Fig. 10b originate in the top right near a ratio of $w_2/w_1 = 2$ as a result of the near linear shape of the contour near the pore. This ratio decreases as distance from the pore increases as the contour rounds toward its maximum width. Higher Reynolds numbers (*i.e.*, higher M) result in narrower dispersions, and thus in curves extending farther to the left in Fig. 10b.

For all M values plotted in Fig. 10b, the curves calculated from Squire's[120] and Gusarov's[125] flow field solutions are similar, indicating agreement of the two solutions on isoconcentration contour shape. The agreement improves as M increases.

C. Experimental jet flows

Figure 11 shows the dye dispersion images obtained for jet cases. Because $Sc >> 1$ for the fluorescein dye and $Re > 1$ in all cases, these flows all correspond to $Pe = ScRe >> 1$. Consequently, dye is transported almost entirely by advection, with diffusion being negligible. Under these conditions, constant concentration contours will approximately follow streamlines in the flow.

Figure 11 superposes selected streamlines from Squire's[120] and Gusarov's[125] jet flow solutions over the experimental images for comparison. For $Re \geq 25$ (Fig. 11b-h), the streamlines follow the dye dispersion edge well for $z \gtrsim 0.5$ mm. The dispersions do not follow the portions of the streamlines along the vertical wall that draw water from the reservoir into the jet, since the dye enters the reservoir through the orifice and is not present away from the hole along the wall.

Deviations from the analytical streamlines very near the pore are attributed to the fact that the

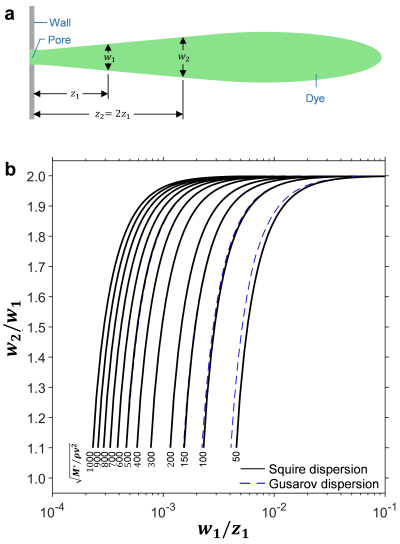

Figure 10: **Summary of isoconcentration contours from high Reynolds number solutions. a** Sketch of dye dispersion geometry outlining a constant concentration contour with definitions of geometric parameters used in panel b. **b** Predicted ratio of isoconcentration contour width at z_1 and $z_2 = 2z_1$. Below each curve, the corresponding value of $\sqrt{M/\rho\nu^2}$ is indicated.

similarity solutions approximate the pore as a point source of momentum, whereas the orifice in the experiment has non-zero diameter. For example, Gusarov's[125] solution corresponds to zero mass flux from the pore, such that in the similarity solution, all streamlines proceed along the vertical wall toward the momentum source and then turn toward the horizontal, entering or following the jet. While entrainment streamlines of this type are a major part of the flow when there is mass flux from the pore, there are also streamlines passing through the pore, directly into the jet. These streamlines are not captured by the similarity solutions, but are present in the experiments and are partly responsible for the difference in the dye dispersion shape from the analytical streamlines near the pore.

The lowest Reynolds number jet observed ($Re = 22$, Fig. 11a) has a much wider spreading angle than streamlines from Squire's[120] and Gusarov's[125] analytical solutions. Since these solutions are for flow created by significant momentum transfer, they do not apply at low Reynolds numbers. By comparison to numerical solutions, Gusarov[126] found good agreement with the analytical solution at $Re = 30$ but not at $Re = 10$. These experimental dye dispersions

Accepted to Phys. Fluids 10.1063/5.0142808

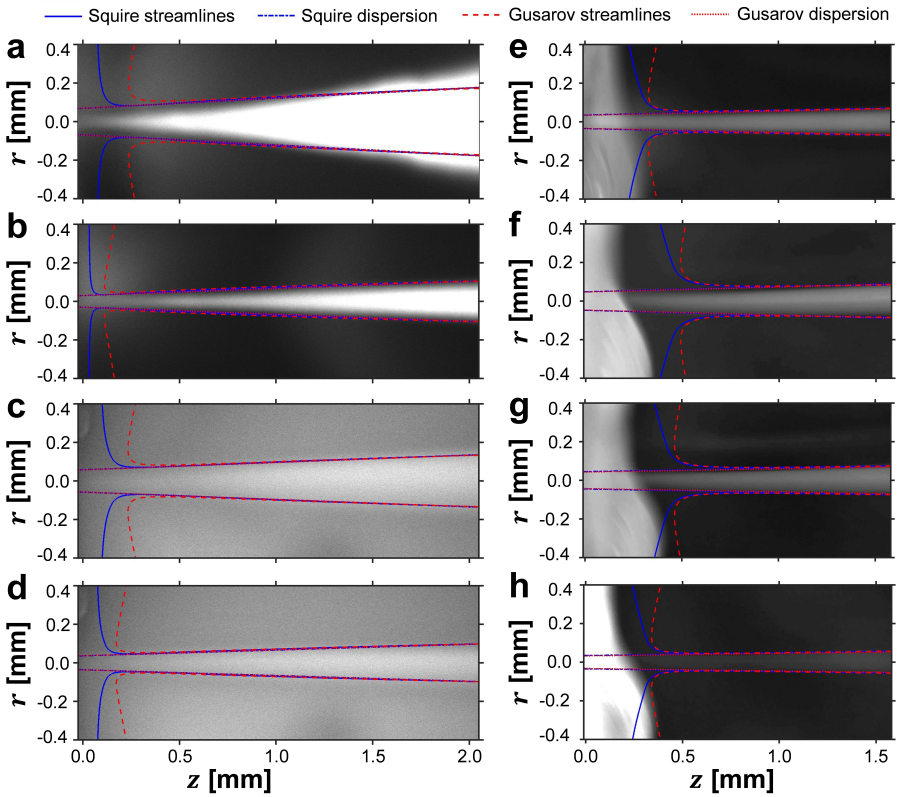

Figure 11: **Jet images with analytical streamlines and isoconcentration contours overlaid. a** $d = 6\,\mu\text{m}$, $\Delta p = 200$ mbar, $Re = 22$. **b** $d = 6\,\mu\text{m}$, $\Delta p = 250$ mbar, $Re = 25$. **c** $d = 50\,\mu\text{m}$, $\Delta p = 6.2$ mbar, $Re = 34$. **d** $d = 50\,\mu\text{m}$, $\Delta p = 9.1$ mbar, $Re = 42$. **e** $d = 50\,\mu\text{m}$, $\Delta p = 39$ mbar, $Re = 89$. **f** $d = 50\,\mu\text{m}$, $\Delta p = 45$ mbar, $Re = 95$. **g** $d = 50\,\mu\text{m}$, $\Delta p = 54$ mbar, $Re = 104$. **h** $d = 50\,\mu\text{m}$, $\Delta p = 63$ mbar, $Re = 113$. Streamlines and isoconcentration contours correspond to $\sqrt{M/\rho\nu^2} = Re$. Isoconcentration contours are shown for $Sc = 2500$ and are offset to a virtual origin upstream of the pore.

are consistent with this finding. The agreement with the high Reynolds number analytical solutions for $Re = 25$ but not at $Re = 22$ provides an estimate of the valid Reynolds number range of these solutions for orifice plate flows. Moreover, this comparison provides further validation for using Squire's[120] or Gusarov's[125] analytical solutions to describe far field jet flow from an orifice plate.

Figure 11 also compares selected constant concentration contours based on Squire's[120] (Eq. 41)

and Gusarov's[125] (from Eq. 40) analytical flow fields with the imaged dye dispersions. Since the similarity solution assumes a point source of dye whereas the experimental flow has a non-zero pore diameter from which dye enters the reservoir, the constant concentration contours are plotted from a virtual origin upstream of the pore to allow some spreading before reaching the pore. This was not necessary when plotting streamlines, because $Sc >> 1$ for fluorescein, such that momentum diffuses away from the point source more rapidly than the dye; the difference in creating a jet from a point source rather than a pore becomes unimportant at a shorter distance from the source for streamlines compared to isoconcentration contours because momentum diffusion away from the source is stronger than mass diffusion. While the constant concentration contours align well with the dye dispersion edge, even near the pore ($z \lesssim 0.5$ mm), at this scale the constant concentration contours are nearly linear. Furthermore, choice of W_0 allows for a wide range of slopes. Thus, while consistent with Eq. 39 and 40, this comparison does not provide strong validation for the derived constant concentration profile shapes.

Although this comparison provides further validation for the use of Squire's[120] and Gusarov's[125] solutions to approximate the far field laminar flow from orifice plates at high Reynolds numbers, the change in streamline shapes with Reynolds number is likely too gradual to resolve small differences in Reynolds numbers from dye dispersion images.

VI. CONCLUSIONS

In this paper we explore the possibility of using microscope images of dye dispersions to measure volume flow rates through small diameter orifice plates. Dye dispersion images show a transition from approximately hemispherical plumes at relatively low Reynolds numbers ($Re \lesssim 10$), to plumes elongated in the axial direction at intermediate Reynolds numbers, and then to narrow jets at higher Reynolds numbers ($Re \gtrsim 20$).

From an approximate solution to the advection-diffusion equation for Sampson's[118] velocity field solution for creeping flow through an orifice plate, we show that at high Péclet number, the concentration field for this flow decays linearly with inverse distance from the pore at large distances, with a slope proportional to the volume flow rate. We further show that the same scaling is predicted from a similarity solution by Gusarov[126] for low Reynolds number flow emerging from a small hole in a plate. We propose to use images of dye plumes to measure the decay of fluorescence intensity with distance from the pore to determine volume flow rate

and validate this approach with images of flow through three micropores of different diameters. Although the approach is derived for $Re << 1$, it is found to provide good results for $Re \lesssim 15$. This is rationalized by an approximate one-dimensional control volume analysis in which dye enters the plume by advection alone, but far from the pore is transported solely by diffusion due to flow spreading and the rapid decay in velocity with distance from the pore.

At higher Reynolds numbers, the velocity remains high in the narrow jet region throughout the field of view. Advection remains significant along the jet axis everywhere in image and the concentration decay rate approach is ineffective. We solved the advection-diffusion equation for the velocity field derived from similarity solutions of Squire[120]and Gusarov[125] for the jet flow emerging from a concentrated momentum source on a wall, with and without slip, respectively. These solutions predict isoconcentration contours ranging from nearly hemispherical to highly elongated for various Reynolds and Schmidt numbers. However, for the Schmidt number of fluorescein dye in these experiments and in the expected range of valid Reynolds numbers for the similarity solutions, the predicted isoconcentration contours are all extremely elongated, providing approximately conical spreading near the pore. Due to the high Péclet number, dye follows streamlines in the flow, and comparison of dye images to streamlines from Gusarov's[125] and Squire's[120] solutions, as well as to the derived isoconcentration contours, show good agreement for $Re \gtrsim 25$. However, precise measurement of volume flow rate by fitting streamlines may be challenging.

The measurement technique validated for lower Reynolds numbers is expected to apply for even smaller pores since it was derived from the flow field for $Re << 1$. Furthermore, we have shown from an approximate control volume analysis that the long range decay of the concentration field at low Reynolds numbers is independent of the geometry of the dye source, provided it is restricted to a finite area in a much larger wall. The method should therefore be suitable for sub-micron pores of arbitrary geometry and to measuring flow through many parallel pores in small areas of membrane materials. The technique adds to the available tools for small scale fluid flow characterization.

ACKNOWLEDGMENTS

This work was funded by the Natural Sciences and Engineering Research Council of Canada (NSERC; Application No. RGPIN-2019-05133; Funder ID: 10.13039/501100000038). This work

made use of equipment purchased through the Natural Sciences and Engineering Research Council of Canada (NSERC) Research Tools and Instruments (RTI) grant program (Application No. RTI-2019-00094; Funder ID: 10.13039/501100000038), Ontario Research Fund (ORF) Small Infrastructure Fund, and Canada Foundation for Innovation (CFI) John R. Evans Leaders Fund (Project No. 39702). Simulations were performed in OpenFOAM[133] using computing resources of the Shared Hierarchical Academic Research Computing Network (SHARCNET: www.sharcnet.ca) and Compute Canada (www.computecanada.ca). This work made use of the Western University Nanofabrication Facility and Surface Science Western.

AUTHOR DECLARATIONS

The authors have no conflicts to disclose.

DATA AVAILABILITY

The data that support the findings of this study are available from the corresponding author upon reasonable request.

REFERENCES

[1]J. Shen, G. Liu, Y. Han, and W. Jin, "Artificial channels for confined mass transport at the sub-nanometre scale," Nature Reviews Materials **6**, 294–312 (2021).

[2]L. Bocquet, "Nanofluidics coming of age," Nature Materials **19**, 254–256 (2020).

[3]Y. Yang, X. Yang, L. Liang, Y. Gao, H. Cheng, X. Li, M. Zou, R. Ma, Q. Yuan, and X. Duan, "Large-area graphene-nanomesh/carbon-nanotube hybrid membranes for ionic and molecular nanofiltration," Science **364**, 1057–1062 (2019).

[4]Y.-x. Shen, W. Song, D. R. Barden, T. Ren, C. Lang, H. Feroz, C. B. Henderson, P. O. Saboe, D. Tsai, H. Yan, P. J. Butler, G. C. Bazan, W. A. Phillip, R. J. Hickey, P. S. Cremer, H. Vashisth, and M. Kumar, "Achieving high permeability and enhanced selectivity for angstrom-scale separations using artificial water channel membranes," Nature Communications **9**, 2294 (2018).

[5]T. Yang, H. Lin, K. P. Loh, and B. Jia, "Fundamental transport mechanisms and advancements of graphene oxide membranes for molecular separation," Chemistry of Materials **31**, 1829–1846 (2019).

[6]S. Sharif, K. S. Ahmad, F. Rehman, Z. Bhatti, and K. H. Thebo, "Two-dimensional graphene oxide based membranes for ionic and molecular separation: Current status and challenges," Journal of Environmental Chemical Engineering **9**, 105605 (2021).

[7]L. Wang, M. S. H. Boutilier, P. R. Kidambi, D. Jang, N. G. Hadjiconstantinou, and R. Karnik, "Fundamental transport mechanisms, fabrication and potential applications of nanoporous atomically thin membranes," Nature Nanotechnology **12**, 509–522 (2017).

[8]L. Prozorovska and P. R. Kidambi, "State-of-the-art and future prospects for atomically thin membranes from 2d materials," Advanced Materials **30**, 1801179 (2018).

[9]M. Sianipar, S. H. Kim, Khoiruddin, F. Iskandar, and I. G. Wenten, "Functionalized carbon nanotube (cnt) membrane: progress and challenges," RSC Adv. **7**, 51175–51198 (2017).

[10]J. S. Roh, H. Lee, T. H. Lee, H. W. Yoon, T. H. Choi, S.-H. Do, S. Y. Yoo, B. D. Freeman, T. Song, U. Paik, and H. B. Park, "Unprecedentedly low co2 transport through vertically aligned, conical silicon nanotube membranes," Nano Letters **20**, 4754–4760 (2020).

[11]R. Das, M. E. Ali, S. B. A. Hamid, S. Ramakrishna, and Z. Z. Chowdhury, "Carbon nanotube membranes for water purification: A bright future in water desalination," Desalination **336**, 97–109 (2014).

[12]J. K. Holt, H. G. Park, Y. Wang, M. Stadermann, A. B. Artyukhin, C. P. Grigoropoulos, A. Noy, and O. Bakajin, "Fast mass transport through sub-2-nanometer carbon nanotubes," Science **312**, 1034–1037 (2006).

[13]F. Fornasiero, "Water vapor transport in carbon nanotube membranes and application in breathable and protective fabrics," Current Opinion in Chemical Engineering **16**, 1–8 (2017), nanotechnology / Separation Engineering.

[14]S. Kim, F. Fornasiero, H. G. Park, J. B. In, E. Meshot, G. Giraldo, M. Stadermann, M. Fireman, J. Shan, C. P. Grigoropoulos, and O. Bakajin, "Fabrication of flexible, aligned carbon nanotube/polymer composite membranes by in-situ polymerization," Journal of Membrane Science **460**, 91–98 (2014).

[15]M. L. Jue, S. F. Buchsbaum, C. Chen, S. J. Park, E. R. Meshot, K. J. J. Wu, and F. Fornasiero, "Ultra-permeable single-walled carbon nanotube membranes with exceptional performance at scale," Advanced Science **7**, 2001670 (2020).

[16]R. L. McGinnis, K. Reimund, J. Ren, L. Xia, M. R. Chowdhury, X. Sun, M. Abril, J. D. Moon, M. M. Merrick, J. Park, K. A. Stevens, J. R. McCutcheon, and B. D. Freeman, "Large-scale polymeric carbon nanotube membranes with sub–1.27-nm pores," Science Advances **4**, e1700938

(2018).

[17]E. Secchi, S. Marbach, A. Niguès, D. Stein, A. Siria, and L. Bocquet, "Massive radius-dependent flow slippage in carbon nanotubes," Nature **537**, 210–213 (2016).

[18]N. Bui, E. R. Meshot, S. Kim, J. Peña, P. W. Gibson, K. J. Wu, and F. Fornasiero, "Ultrabreathable and protective membranes with sub-5 nm carbon nanotube pores," Advanced Materials **28**, 5871–5877 (2016).

[19]S. P. Koenig, L. Wang, J. Pellegrino, and J. S. Bunch, "Selective molecular sieving through porous graphene," Nature Nanotechnology **7**, 728–732 (2012).

[20]T. Jain, B. C. Rasera, R. J. S. Guerrero, M. S. H. Boutilier, S. C. O'Hern, J.-C. Idrobo, and R. Karnik, "Heterogeneous sub-continuum ionic transport in statistically isolated graphene nanopores," Nature Nanotechnology **10**, 1053–1057 (2015).

[21]L. Cantley, J. L. Swett, D. Lloyd, D. A. Cullen, K. Zhou, P. V. Bedworth, S. Heise, A. J. Rondinone, Z. Xu, S. Sinton, and J. S. Bunch, "Voltage gated inter-cation selective ion channels from graphene nanopores," Nanoscale **11**, 9856–9861 (2019).

[22]R. C. Rollings, A. T. Kuan, and J. A. Golovchenko, "Ion selectivity of graphene nanopores," Nature Communications **7**, 11408 (2016).

[23]S. C. O'Hern, M. S. H. Boutilier, J.-C. Idrobo, Y. Song, J. Kong, T. Laoui, M. Atieh, and R. Karnik, "Selective ionic transport through tunable subnanometer pores in single-layer graphene membranes," Nano Letters **14**, 1234–1241 (2014).

[24]M. S. H. Boutilier, D. Jang, J.-C. Idrobo, P. R. Kidambi, N. G. Hadjiconstantinou, and R. Karnik, "Molecular sieving across centimeter-scale single-layer nanoporous graphene membranes," ACS Nano **11**, 5726–5736 (2017).

[25]M. S. H. Boutilier, N. G. Hadjiconstantinou, and R. Karnik, "Knudsen effusion through polymer-coated three-layer porous graphene membranes," Nanotechnology **28**, 184003 (2017).

[26]D. Jang, J.-C. Idrobo, T. Laoui, and R. Karnik, "Water and solute transport governed by tunable pore size distributions in nanoporous graphene membranes," ACS Nano **11**, 10042–10052 (2017).

[27]P. Cheng, M. M. Kelly, N. K. Moehring, W. Ko, A.-P. Li, J. C. Idrobo, M. S. H. Boutilier, and P. R. Kidambi, "Facile size-selective defect sealing in large-area atomically thin graphene membranes for sub-nanometer scale separations," Nano Letters **20**, 5951–5959 (2020).

[28]P. Cheng, F. Fornasiero, M. L. Jue, W. Ko, A.-P. Li, J. C. Idrobo, M. S. H. Boutilier, and P. R. Kidambi, "Differences in water and vapor transport through angstrom-scale pores in

atomically thin membranes," Nature Communications **13**, 6709 (2022).

[29]C. Cheng, S. A. Iyengar, and R. Karnik, "Molecular size-dependent subcontinuum solvent permeation and ultrafast nanofiltration across nanoporous graphene membranes," Nature Nanotechnology **16**, 989–995 (2021).

[30]S. P. Surwade, S. N. Smirnov, I. V. Vlassiouk, R. R. Unocic, G. M. Veith, S. Dai, and S. M. Mahurin, "Water desalination using nanoporous single-layer graphene," Nature Nanotechnology **10**, 459–464 (2015).

[31]K. Celebi, J. Buchheim, R. M. Wyss, A. Droudian, P. Gasser, I. Shorubalko, J.-I. Kye, C. Lee, and H. G. Park, "Ultimate permeation across atomically thin porous graphene," Science **344**, 289–292 (2014).

[32]L. Shen, Q. Shi, S. Zhang, J. Gao, D. C. Cheng, M. Yi, R. Song, L. Wang, J. Jiang, R. Karnik, and S. Zhang, "Highly porous nanofiber-supported monolayer graphene membranes for ultrafast organic solvent nanofiltration," Science Advances **7**, eabg6263 (2021).

[33]S. Huang, M. Dakhchoune, W. Luo, E. Oveisi, G. He, M. Rezaei, J. Zhao, D. T. L. Alexander, A. Züttel, M. S. Strano, and K. V. Agrawal, "Single-layer graphene membranes by crack-free transfer for gas mixture separation," Nature Communications **9**, 2632 (2018).

[34]W.-C. Lee, L. Bondaz, S. Huang, G. He, M. Dakhchoune, and K. V. Agrawal, "Centimeter-scale gas-sieving nanoporous single-layer graphene membrane," Journal of Membrane Science **618**, 118745 (2021).

[35]M. H. Khan, M. Moradi, M. Dakhchoune, M. Rezaei, S. Huang, J. Zhao, and K. V. Agrawal, "Hydrogen sieving from intrinsic defects of benzene-derived single-layer graphene," Carbon **153**, 458–466 (2019).

[36]Z. Yuan, G. He, S. Faucher, M. Kuehne, S. X. Li, D. Blankschtein, and M. S. Strano, "Direct chemical vapor deposition synthesis of porous single-layer graphene membranes with high gas permeances and selectivities," Advanced Materials **33**, 2104308 (2021).

[37]K.-P. Schlichting and D. Poulikakos, "Selective etching of graphene membrane nanopores: From molecular sieving to extreme permeance," ACS Applied Materials & Interfaces **12**, 36468–36477 (2020).

[38]J. Zhao, G. He, S. Huang, L. F. Villalobos, M. Dakhchoune, H. Bassas, and K. V. Agrawal, "Etching gas-sieving nanopores in single-layer graphene with an angstrom precision for high-performance gas mixture separation," Science Advances **5**, eaav1851 (2019).

[39]H. W. Kim, H. W. Yoon, S.-M. Yoon, B. M. Yoo, B. K. Ahn, Y. H. Cho, H. J. Shin, H. Yang, U. Paik, S. Kwon, J.-Y. Choi, and H. B. Park, "Selective gas transport through few-layered graphene and graphene oxide membranes," Science **342**, 91–95 (2013).

[40]H. Li, Z. Song, X. Zhang, Y. Huang, S. Li, Y. Mao, H. J. Ploehn, Y. Bao, and M. Yu, "Ultrathin, molecular-sieving graphene oxide membranes for selective hydrogen separation," Science **342**, 95–98 (2013).

[41]I. Chandio, F. A. Janjhi, A. A. Memon, S. Memon, Z. Ali, K. H. Thebo, A. A. A. Pirzado, A. A. Hakro, and W. S. Khan, "Ultrafast ionic and molecular sieving through graphene oxide based composite membranes," Desalination **500**, 114848 (2021).

[42]A. P. Straub, D. S. Bergsman, B. A. Getachew, L. M. Leahy, J. J. Patil, N. Ferralis, and J. C. Grossman, "Highly conductive and permeable nanocomposite ultrafiltration membranes using laser-reduced graphene oxide," Nano Letters **21**, 2429–2435 (2021).

[43]P. Su, F. Wang, Z. Li, C. Y. Tang, and W. Li, "Graphene oxide membranes: controlling their transport pathways," J. Mater. Chem. A **8**, 15319–15340 (2020).

[44]S. Wang, L. Yang, G. He, B. Shi, Y. Li, H. Wu, R. Zhang, S. Nunes, and Z. Jiang, "Two-dimensional nanochannel membranes for molecular and ionic separations," Chem. Soc. Rev. **49**, 1071–1089 (2020).

[45]K. H. Thebo, X. Qian, Q. Zhang, L. Chen, H.-M. Cheng, and W. Ren, "Highly stable graphene-oxide-based membranes with superior permeability," Nature Communications **9**, 1486 (2018).

[46]Q. Zhang, X. Qian, K. H. Thebo, H.-M. Cheng, and W. Ren, "Controlling reduction degree of graphene oxide membranes for improved water permeance," Science Bulletin **63**, 788–794 (2018).

[47]J. Y. Chong, B. Wang, C. Mattevi, and K. Li, "Dynamic microstructure of graphene oxide membranes and the permeation flux," Journal of Membrane Science **549**, 385–392 (2018).

[48]J. Liu, N. Wang, L.-J. Yu, A. Karton, W. Li, W. Zhang, F. Guo, L. Hou, Q. Cheng, L. Jiang, D. A. Weitz, and Y. Zhao, "Bioinspired graphene membrane with temperature tunable channels for water gating and molecular separation," Nature Communications **8**, 2011 (2017).

[49]L. Chen, G. Shi, J. Shen, B. Peng, B. Zhang, Y. Wang, F. Bian, J. Wang, D. Li, Z. Qian, G. Xu, G. Liu, J. Zeng, L. Zhang, Y. Yang, G. Zhou, M. Wu, W. Jin, J. Li, and H. Fang, "Ion sieving in graphene oxide membranes via cationic control of interlayer spacing," Nature **550**, 380–383 (2017).

[50]Z. Zhou, Y. Tan, Q. Yang, A. Bera, Z. Xiong, M. Yagmurcukardes, M. Kim, Y. Zou, G. Wang, A. Mishchenko, I. Timokhin, C. Wang, H. Wang, C. Yang, Y. Lu, R. Boya, H. Liao, S. Haigh, H. Liu, F. M. Peeters, Y. Li, A. K. Geim, and S. Hu, "Gas permeation through graphdiyne-based nanoporous membranes," Nature Communications **13**, 4031 (2022).

[51]Z. Ahmed, F. Rehman, U. Ali, A. Ali, M. Iqbal, and K. H. Thebo, "Recent advances in mxene-based separation membranes," ChemBioEng Reviews **8**, 110–120 (2021).

[52]D. I. Petukhov, A. S. Kan, A. P. Chumakov, O. V. Konovalov, R. G. Valeev, and A. A. Eliseev, "Mxene-based gas separation membranes with sorption type selectivity," Journal of Membrane Science **621**, 118994 (2021).

[53]C. Fan, L. Cao, C. Yang, Q. Xiao, X. You, X. Wang, Y. Kong, H. Wu, Y. Liu, and Z. Jiang, "Charged nanochannels endow cof membrane with weakly concentration-dependent methanol permeability," Journal of Membrane Science **645**, 120186 (2022).

[54]R. Shevate and D. L. Shaffer, "Large-area 2d covalent organic framework membranes with tunable single-digit nanopores for predictable mass transport," ACS Nano **16**, 2407–2418 (2022).

[55]H. Yang, L. Yang, H. Wang, Z. Xu, Y. Zhao, Y. Luo, N. Nasir, Y. Song, H. Wu, F. Pan, and Z. Jiang, "Covalent organic framework membranes through a mixed-dimensional assembly for molecular separations," Nature Communications **10**, 2101 (2019).

[56]P. Cheng, Y. Huang, C. Wu, X. Wang, X. Fu, P. Li, Y. Liu, and S. Xia, "Two-dimensional metal-porphyrin framework membranes for efficient molecular sieving," Journal of Membrane Science **640**, 119812 (2021).

[57]S. C. O'Hern, C. A. Stewart, M. S. H. Boutilier, J.-C. Idrobo, S. Bhaviripudi, S. K. Das, J. Kong, T. Laoui, M. Atieh, and R. Karnik, "Selective molecular transport through intrinsic defects in a single layer of cvd graphene," ACS Nano **6**, 10130–10138 (2012).

[58]M. S. H. Boutilier, C. Sun, S. C. O'Hern, H. Au, N. G. Hadjiconstantinou, and R. Karnik, "Implications of permeation through intrinsic defects in graphene on the design of defect-tolerant membranes for gas separation," ACS Nano **8**, 841–849 (2014).

[59]R. Rao, C. L. Pint, A. E. Islam, R. S. Weatherup, S. Hofmann, E. R. Meshot, F. Wu, C. Zhou, N. Dee, P. B. Amama, J. Carpena-Nuñez, W. Shi, D. L. Plata, E. S. Penev, B. I. Yakobson, P. B. Balbuena, C. Bichara, D. N. Futaba, S. Noda, H. Shin, K. S. Kim, B. Simard, F. Mirri, M. Pasquali, F. Fornasiero, E. I. Kauppinen, M. Arnold, B. A. Cola, P. Nikolaev, S. Arepalli, H.-M. Cheng, D. N. Zakharov, E. A. Stach, J. Zhang, F. Wei, M. Terrones, D. B. Geohegan, B. Maruyama, S. Maruyama, Y. Li, W. W. Adams, and A. J. Hart, "Carbon nanotubes and related nanomaterials:

Critical advances and challenges for synthesis toward mainstream commercial applications," ACS Nano **12**, 11756–11784 (2018).

[60]L. Bocquet and P. Tabeling, "Physics and technological aspects of nanofluidics," Lab on a Chip **14**, 3143–3158 (2014).

[61]S. Faucher, N. Aluru, M. Z. Bazant, D. Blankschtein, A. H. Brozena, J. Cumings, J. Pedro de Souza, M. Elimelech, R. Epsztein, J. T. Fourkas, A. G. Rajan, H. J. Kulik, A. Levy, A. Majumdar, C. Martin, M. McEldrew, R. P. Misra, A. Noy, T. A. Pham, M. Reed, E. Schwegler, Z. Siwy, Y. Wang, and M. Strano, "Critical knowledge gaps in mass transport through single-digit nanopores: A review and perspective," The Journal of Physical Chemistry C **123**, 21309–21326 (2019).

[62]N. Kavokine, R. R. Netz, and L. Bocquet, "Fluids at the nanoscale: From continuum to subcontinuum transport," Annual Review of Fluid Mechanics **53**, 377–410 (2021).

[63]M. E. Suk and N. R. Aluru, "Molecular and continuum hydrodynamics in graphene nanopores," RSC Adv. **3**, 9365–9372 (2013).

[64]D. Cohen-Tanugi and J. C. Grossman, "Water desalination across nanoporous graphene," Nano Letters **12**, 3602–3608 (2012).

[65]J.-G. Gai and X.-L. Gong, "Zero internal concentration polarization fo membrane: functionalized graphene," J. Mater. Chem. A **2**, 425–429 (2014).

[66]J.-G. Gai, X.-L. Gong, W.-W. Wang, X. Zhang, and W.-L. Kang, "An ultrafast water transport forward osmosis membrane: porous graphene," J. Mater. Chem. A **2**, 4023–4028 (2014).

[67]M. Heiranian, A. B. Farimani, and N. R. Aluru, "Water desalination with a single-layer mos2 nanopore," Nature Communications **6**, 8616 (2015).

[68]C. Zhu, H. Li, X. C. Zeng, E. G. Wang, and S. Meng, "Quantized water transport: Ideal desalination through graphyne-4 membrane," Scientific Reports **3**, 3163 (2013).

[69]M. Xue, H. Qiu, and W. Guo, "Exceptionally fast water desalination at complete salt rejection by pristine graphyne monolayers," Nanotechnology **24**, 505720 (2013).

[70]J. Kou, X. Zhou, Y. Chen, H. Lu, F. Wu, and J. Fan, "Water permeation through single-layer graphyne membrane," The Journal of Chemical Physics **139**, 064705 (2013).

[71]L.-C. Lin, J. Choi, and J. C. Grossman, "Two-dimensional covalent triazine framework as an ultrathin-film nanoporous membrane for desalination," Chem. Commun. **51**, 14921–14924 (2015).

[72]Z. Song and Z. Xu, "Ultimate osmosis engineered by the pore geometry and functionalization of carbon nanostructures," Scientific Reports **5**, 10597 (2015).

[73]S. Lin and M. J. Buehler, "Mechanics and molecular filtration performance of graphyne nanoweb membranes for selective water purification," Nanoscale **5**, 11801–11807 (2013).

[74]J. Kou, X. Zhou, H. Lu, F. Wu, and J. Fan, "Graphyne as the membrane for water desalination," Nanoscale **6**, 1865–1870 (2014).

[75]D. Cohen-Tanugi, L.-C. Lin, and J. C. Grossman, "Multilayer nanoporous graphene membranes for water desalination," Nano Letters **16**, 1027–1033 (2016).

[76]D. Cohen-Tanugi and J. C. Grossman, "Water permeability of nanoporous graphene at realistic pressures for reverse osmosis desalination," The Journal of Chemical Physics **141**, 074704 (2014).

[77]C. Sun, M. S. H. Boutilier, H. Au, P. Poesio, B. Bai, R. Karnik, and N. G. Hadjiconstantinou, "Mechanisms of molecular permeation through nanoporous graphene membranes," Langmuir **30**, 675–682 (2014).

[78]M. E. Suk and N. R. Aluru, "Water transport through ultrathin graphene," The Journal of Physical Chemistry Letters **1**, 1590–1594 (2010).

[79]J. Yang, Z. Shen, J. He, and Y. Li, "Efficient separation of small organic contaminants in water using functionalized nanoporous graphene membranes: Insights from molecular dynamics simulations," Journal of Membrane Science **630**, 119331 (2021).

[80]Y. Wang, Z. He, K. M. Gupta, Q. Shi, and R. Lu, "Molecular dynamics study on water desalination through functionalized nanoporous graphene," Carbon **116**, 120–127 (2017).

[81]V. P. K., S. K. Kannam, R. Hartkamp, and S. P. Sathian, "Water desalination using graphene nanopores: influence of the water models used in simulations," Physical Chemistry Chemical Physics **20**, 16005–16011 (2018).

[82]J. Schrier, "Helium separation using porous graphene membranes," The Journal of Physical Chemistry Letters **1**, 2284–2287 (2010).

[83]S. Blankenburg, M. Bieri, R. Fasel, K. Müllen, C. A. Pignedoli, and D. Passerone, "Porous graphene as an atmospheric nanofilter," Small **6**, 2266–2271 (2010).

[84]J. Schrier and J. McClain, "Thermally-driven isotope separation across nanoporous graphene," Chemical Physics Letters **521**, 118–124 (2012).

[85]D.-e. Jiang, V. R. Cooper, and S. Dai, "Porous graphene as the ultimate membrane for gas separation," Nano Letters **9**, 4019–4024 (2009).

[86]J. Schrier, "Carbon dioxide separation with a two-dimensional polymer membrane," ACS Applied Materials & Interfaces **4**, 3745–3752 (2012).

[87]Y. Tao, Q. Xue, Z. Liu, M. Shan, C. Ling, T. Wu, and X. Li, "Tunable hydrogen separation in porous graphene membrane: First-principle and molecular dynamic simulation," ACS Applied Materials & Interfaces **6**, 8048–8058 (2014).

[88]K. Solvik, J. A. Weaver, A. M. Brockway, and J. Schrier, "Entropy-driven molecular separations in 2d-nanoporous materials, with application to high-performance paraffin/olefin membrane separations," The Journal of Physical Chemistry C **117**, 17050–17057 (2013).

[89]H. Liu, S. Dai, and D.-e. Jiang, "Permeance of h2 through porous graphene from molecular dynamics," Solid State Communications **175-176**, 101–105 (2013).

[90]Y. Jiao, A. Du, M. Hankel, and S. C. Smith, "Modelling carbon membranes for gas and isotope separation," Physical Chemistry Chemical Physics **15**, 4832–4843 (2013).

[91]L. W. Drahushuk and M. S. Strano, "Mechanisms of gas permeation through single layer graphene membranes," Langmuir **28**, 16671–16678 (2012).

[92]A. O. Wong, H. K. Atwal, and M. S. Boutilier, "Molecular advection–diffusion through graphene nanopores," European Journal of Mechanics - B/Fluids **94**, 366–374 (2022).

[93]G. Yilmaz and S. Keskin, "Predicting the performance of zeolite imidazolate framework/polymer mixed matrix membranes for co2, ch4, and h2 separations using molecular simulations," Industrial & Engineering Chemistry Research **51**, 14218–14228 (2012).

[94]Y. Zhang, T. Fang, Q. Hou, Z. Li, and Y. Yan, "Water desalination of a new three-dimensional covalent organic framework: a molecular dynamics simulation study," Physical Chemistry Chemical Physics **22**, 16978–16984 (2020).

[95]L. Liu, Y. Liu, Y. Qi, M. Song, L. Jiang, G. Fu, and J. Li, "Hexagonal boron nitride with nanoslits as a membrane for water desalination: A molecular dynamics investigation," Separation and Purification Technology **251**, 117409 (2020).

[96]L. Li, T. Zhang, Y. Duan, Y. Wei, C. Dong, L. Ding, Z. Qiao, and H. Wang, "Selective gas diffusion in two-dimensional mxene lamellar membranes: insights from molecular dynamics simulations," Journal of Materials Chemistry A **6**, 11734–11742 (2018).

[97]C. Sun, M. Liu, and B. Bai, "Molecular simulations on graphene-based membranes," Carbon **153**, 481–494 (2019).

[98]T. Tran-Duc, N. Phan-Thien, and J. Wang, "A theoretical study of permeability enhancement for ultrafiltration ceramic membranes with conical pores and slippage," Physics of Fluids **31**,

022003 (2019).

[99]X. Chen, Y. Jian, and Z. Xie, "Electrokinetic flow of fluids with pressure-dependent viscosity in a nanotube," Physics of Fluids **33**, 122002 (2021).

[100]Y. Jin, X. Gao, K. Zhang, and Z. Li, "A nanopump using carbon nanotube hetero-junction driven by symmetric temperature gradients," Physics of Fluids **33**, 082001 (2021).

[101]T. F. Viscondi, A. Grigolo, I. L. Caldas, and J. R. Meneghini, "Slippery-sticky transition of interfacial fluid slip," Physics of Fluids **33**, 062012 (2021).

[102]A. Zou and S. C. Maroo, "Nano-confinement effects on liquid pressure," Physics of Fluids **33**, 042007 (2021).

[103]C. Sun, R. Zhou, and B. Bai, "How to accurately predict nanoscale flow: Theory of single-phase or two-phase?" Physics of Fluids **35**, 012013 (2023).

[104]O. I. Vinogradova, E. F. Silkina, and E. S. Asmolov, "Transport of ions in hydrophobic nanotubes," Physics of Fluids **34**, 122003 (2022).

[105]Q. Guan, B. Shan, R. Wang, G. Feng, and Z. Guo, "Evaluation of different particle-actuation modes in molecular dynamics and their impact on nanoscale flow behaviors," Physics of Fluids **34**, 072006 (2022).

[106]S. Chanda and P. A. Tsai, "Competition between electroosmotic and chemiosmotic flow in charged nanofluidics," Physics of Fluids **33**, 032008 (2021).

[107]J. Feng, M. Graf, K. Liu, D. Ovchinnikov, D. Dumcenco, M. Heiranian, V. Nandigana, N. R. Aluru, A. Kis, and A. Radenovic, "Single-layer mos2 nanopores as nanopower generators," Nature **536**, 197–200 (2016).

[108]J. Geng, K. Kim, J. Zhang, A. Escalada, R. Tunuguntla, L. R. Comolli, F. I. Allen, A. V. Shnyrova, K. R. Cho, D. Munoz, Y. M. Wang, C. P. Grigoropoulos, C. M. Ajo-Franklin, V. A. Frolov, and A. Noy, "Stochastic transport through carbon nanotubes in lipid bilayers and live cell membranes," Nature **514**, 612–615 (2014).

[109]J. S. Bunch, S. S. Verbridge, J. S. Alden, A. M. van der Zande, J. M. Parpia, H. G. Craighead, and P. L. McEuen, "Impermeable atomic membranes from graphene sheets," Nano Letters **8**, 2458–2462 (2008).

[110]L. Wang, L. W. Drahushuk, L. Cantley, S. P. Koenig, X. Liu, J. Pellegrino, M. S. Strano, and J. Scott Bunch, "Molecular valves for controlling gas phase transport made from discrete ångström-sized pores in graphene," Nature Nanotechnology **10**, 785–790 (2015).

[111]N. Laohakunakorn, B. Gollnick, F. Moreno-Herrero, D. G. A. L. Aarts, R. P. A. Dullens, S. Ghosal, and U. F. Keyser, "A landau–squire nanojet," Nano Letters **13**, 5141–5146 (2013).

[112]E. Secchi, S. Marbach, A. Niguès, A. Siria, and L. Bocquet, "The landau–squire plume," Journal of Fluid Mechanics **826**, R3 (2017), r3.

[113]K. Mathwig, D. Mampallil, S. Kang, and S. G. Lemay, "Electrical cross-correlation spectroscopy: Measuring picoliter-per-minute flows in nanochannels," Phys. Rev. Lett. **109**, 118302 (2012).

[114]C. Kuang and G. Wang, "A novel far-field nanoscopic velocimetry for nanofluidics," Lab on a Chip **10**, 240–245 (2010).

[115]G. R. Wang, "Laser induced fluorescence photobleaching anemometer for microfluidic devices," Lab on a Chip **5**, 450–456 (2005).

[116]H. B. Squire, "The Round Laminar Jet," The Quarterly Journal of Mechanics and Applied Mathematics **4**, 321–329 (1951).

[117]L. D. Landau and E. M. Lifshitz, *Fluid Mechanics, Second Edition (Translated from the Russian by J.B. Sykes and W.H. Reid)* (Pergamon Press, 1959).

[118]R. A. Sampson, "On Stokes's current function," Philosophical Transactions of the Royal Society A **182**, 449–518 (1891).

[119]H. K. Atwal, A. O. K. Wong, and M. S. H. Boutilier, "Mass Advection–Diffusion in Creeping Flow Through an Orifice Plate: A Model for Nanoporous Atomically Thin Membranes," Journal of Heat Transfer **144** (2022), 10.1115/1.4053041.

[120]H. Squire, "Xci. some viscous fluid flow problems i: Jet emerging from a hole in a plane wall," The London, Edinburgh, and Dublin Philosophical Magazine and Journal of Science **43**, 942–945 (1952).

[121]V. I. Yatseyev, "On a class of exact solution of the equations of motion of a viscous fluid," Tech. Rep. (National Advisory Committee for Aeronautics, 1950).

[122]M. Beran, "A note on laminar axially symmetric jets," Quarterly of Applied Mathematics **14**, 213–214 (1956).

[123]W. Schneider, "Flow induced by jets and plumes," Journal of Fluid Mechanics **108**, 55–65 (1981).

[124]W. Schneider, "Decay of momentum flux in submerged jets," Journal of Fluid Mechanics **154**, 91–110 (1985).

[125]A. V. Gusarov, "Analytic similarity solutions of the navier–stokes equations for a jet in a half space with the no-slip boundary condition," Physics of Fluids **32**, 053104 (2020).

[126]A. V. Gusarov, "Entrainment flow of a jet emerging into a half-space with the no-slip boundary condition," Physics of Fluids **32**, 083107 (2020).

[127]F. C. Johansen and R. V. Southwell, "Flow through pipe orifices at low reynolds numbers," Proceedings of the Royal Society of London. Series A, Containing Papers of a Mathematical and Physical Character **126**, 231–245 (1930).

[128]F. Kusmanto, E. L. Jacobsen, and B. A. Finlayson, "Applicability of continuum mechanics to pressure drop in small orifices," Physics of Fluids **16**, 4129–4134 (2004).

[129]F. M. White, *Fluid Mechanics, Sixth Edition* (McGraw-Hill, 2008).

[130]D. Phares, G. Smedley, and J. Zhou, "Laminar flow resistance in short microtubes," International Journal of Heat and Fluid Flow **26**, 506–512 (2005).

[131]T. Hasegawa, M. Suganuma, and H. Watanabe, "Anomaly of excess pressure drops of the flow through very small orifices," Physics of Fluids **9**, 1–3 (1997).

[132]W. N. Bond, "The effect of viscosity on orifice flows," Proceedings of the Physical Society of London **33**, 225 (1920).

[133]H. G. Weller, G. Tabor, H. Jasak, and C. Fureby, "A tensorial approach to computational continuum mechanics using object-oriented techniques," Computers in Physics **12**, 620–631 (1998).

[134]Z. Dagan, S. Weinbaum, and R. Pfeffer, "An infinite-series solution for the creeping motion through an orifice of finite length," Journal of Fluid Mechanics **115**, 505–523 (1982).

[135]E. N. Lightfoot, R. B. Bird, and W. E. Stewart, *Transport Phenomena, Revised 2nd Edition* (John Wiley and Sons, 2006).

[136]H. F. Bauer, "Mass transport in a converging-diverging nozzle," Wärme - und Stoffübertragung **22**, 201–208 (1988).

[137]G. B. Arfken and H. J. Weber, *Mathematical Methods for Physicists, Sixth Edition* (Elsevier Academic Press, 2005).

[138]R. M. Cotta, *Integral Transforms in Computational Heat and Fluid Flow* (CRC Press, 1993).

[139]J. C. Waters, "Accuracy and precision in quantitative fluorescence microscopy," Journal of Cell Biology **185**, 1135–1148 (2009).

[140]C. T. Culbertson, S. C. Jacobson, and J. Michael Ramsey, "Diffusion coefficient measurements in microfluidic devices," Talanta **56**, 365–373 (2002).